

## CONSTRAINING COSMIC EVOLUTION OF TYPE IA SUPERNOVAE

RYAN J. FOLEY<sup>1</sup>, ALEXEI V. FILIPPENKO<sup>1</sup>, C. AGUILERA<sup>2</sup>, A. C. BECKER<sup>3</sup>, S. BLONDIN<sup>4</sup>, P. CHALLIS<sup>4</sup>, A. CLOCCHIATTI<sup>5</sup>, R. COVARRUBIAS<sup>3</sup>, T. M. DAVIS<sup>6</sup>, P. M. GARNAVICH<sup>7</sup>, S. JHA<sup>1,8</sup>, R. P. KIRSHNER<sup>4</sup>, K. KRISCIUNAS<sup>9</sup>, B. LEIBUNDGUT<sup>10</sup>, W. LI<sup>1</sup>, T. MATHESON<sup>11</sup>, A. MICELI<sup>3</sup>, G. MIKNAITIS<sup>12</sup>, G. PIGNATA<sup>13</sup>, A. REST<sup>2,14</sup>, A. G. RIESS<sup>15,16</sup>, B. P. SCHMIDT<sup>17</sup>, R. C. SMITH<sup>2</sup>, J. SOLLERMAN<sup>6,18</sup>, J. SPYROMILIO<sup>10</sup>, C. W. STUBBS<sup>4,14</sup>, J. L. TONRY<sup>19</sup>, N. B. SUNTZEFF<sup>2,9</sup>, W. M. WOOD-VASEY<sup>4</sup>, AND A. ZENTENO<sup>20</sup>

*Draft version February 2, 2008*

### ABSTRACT

We present the first large-scale effort of creating composite spectra of high-redshift type Ia supernovae (SNe Ia) and comparing them to low-redshift counterparts. Through the ESSENCE project, we have obtained 107 spectra of 88 high-redshift SNe Ia with excellent light-curve information. In addition, we have obtained 397 spectra of low-redshift SNe Ia through a multiple-decade effort at Lick and Keck Observatories, and we have used 45 ultraviolet spectra obtained by *HST/IUE*. The low-redshift spectra act as a control sample when comparing to the ESSENCE spectra. In all instances, the ESSENCE and Lick composite spectra appear very similar. The addition of galaxy light to the Lick composite spectra allows a nearly perfect match of the overall spectral-energy distribution with the ESSENCE composite spectra, indicating that the high-redshift SNe are more contaminated with host-galaxy light than their low-redshift counterparts. This is caused by observing objects at all redshifts with similar slit widths, which corresponds to different projected distances. After correcting for the galaxy-light contamination, subtle differences in the spectra remain. We have estimated the systematic errors when using current spectral templates for K-corrections to be  $\sim 0.02$  mag. The variance in the composite spectra give an estimate of the intrinsic variance in low-redshift maximum-light SN spectra of  $\sim 3\%$  in the optical and growing toward the ultraviolet. The difference between the maximum-light low and high-redshift spectra constrain SN evolution between our samples to be  $< 10\%$  in the rest-frame optical.

*Subject headings:* supernovae: general — cosmology: observations — cosmology — distance scale

### 1. INTRODUCTION

Type Ia supernovae (SNe Ia) are the most precise known distance indicators at cosmological redshifts. The meticulous measurement of several hundred SNe Ia at both low and high redshifts has shown that the expansion of the Universe is currently accelerating (Riess et al. 1998, 2007; Perlmutter et al. 1999; Astier et al. 2006; Wood-Vasey et al. 2007); see Filippenko (2005) for a recent review. The underlying assumption behind that work is that high-redshift SNe Ia have the same peak luminosity as low-redshift SNe Ia (after corrections based on light-curve shape; e.g., Phillips 1993). The luminosity of a given SN and its light-curve shape are determined by initial conditions of the white dwarf progenitor star (e.g., mass at explosion, C/O abundance, and metallicity), and the properties of the explosion (e.g., deflagration/detonation transition, the amount of unburned material, and the density at the ignition point). The progenitor properties are set by the initial conditions at the formation of the progenitor system, presumably having properties similar to the global galactic properties at that time. Since low-redshift SN Ia progenitor systems likely form, on average, in significantly different environments than high-redshift SN Ia progenitors, one may assume that some amount of evolution is inevitable (for a dis-

Electronic address: rfoley@astro.berkeley.edu

<sup>1</sup> Department of Astronomy, 601 Campbell Hall, University of California, Berkeley, CA 94720-3411

<sup>2</sup> Cerro Tololo Inter-American Observatory, Casilla 603, La Serena, Chile

<sup>3</sup> Department of Astronomy, University of Washington, Box 351580, Seattle, WA 98195-1580

<sup>4</sup> Harvard-Smithsonian Center for Astrophysics, 60 Garden Street, Cambridge, MA 02138

<sup>5</sup> Pontificia Universidad Católica de Chile, Departamento de Astronomía y Astrofísica, Casilla 306, Santiago 22, Chile

<sup>6</sup> Dark Cosmology Centre, Niels Bohr Institute, University of Copenhagen, Juliane Maries Vej 30, DK-2100 Copenhagen Ø, Denmark

<sup>7</sup> Department of Physics, University of Notre Dame, 225 Nieuwland Science Hall, Notre Dame, IN 46556-5670

<sup>8</sup> Kavli Institute for Particle Astrophysics and Cosmology, Stanford Linear Accelerator Center, 2575 Sand Hill Road, MS 29, Menlo Park, CA 94025

<sup>9</sup> Department of Physics, Texas A&M University, College Station, TX 77843-4242

<sup>10</sup> European Southern Observatory, Karl-Schwarzschild-Strasse 2, D-85748 Garching, Germany

<sup>11</sup> National Optical Astronomy Observatory, 950 North Cherry Avenue, Tucson, AZ 85719-4933

<sup>12</sup> Fermilab, P.O. Box 500, Batavia, IL 60510-0500

<sup>13</sup> Departamento de Astronomía, Universidad de Chile, Casilla 36-D, Santiago, Chile

<sup>14</sup> Department of Physics, Harvard University, 17 Oxford Street, Cambridge, MA 02138

<sup>15</sup> Space Telescope Science Institute, 3700 San Martin Drive, Baltimore, MD 21218

<sup>16</sup> Johns Hopkins University, 3400 North Charles Street, Baltimore, MD 21218

<sup>17</sup> The Research School of Astronomy and Astrophysics, The Australian National University, Mount Stromlo and Siding Spring Observatories, via Cotter Road, Weston Creek, PO 2611, Australia

<sup>18</sup> Department of Astronomy, Stockholm University, AlbaNova,

10691 Stockholm, Sweden

<sup>19</sup> Institute for Astronomy, University of Hawaii, 2680 Woodlawn Drive, Honolulu, HI 96822

<sup>20</sup> Univ. of Illinois, Dept. of Astronomy, 1002 W. Green St., Urbana, IL 61801

cussion of different causes and effects of SN evolution, see Leibundgut 2001).

Theoretical studies of SN Ia evolution have focused on the composition, particularly metallicity, of the progenitor system as the primary potential difference between the two samples. There have been two major studies with conflicting results. For their study, Höflich et al. (1998) changed the progenitor metallicity and modeled the explosion, including a full nuclear-reaction network. Lentz et al. (2000) changed the metallicity of the results of W7 models (Nomoto et al. 1984) and input those parameters into their PHOENIX code (Hauschildt et al. 1996) to produce synthetic spectra. The main difference between these methods is the definition of “metallicity.” Höflich et al. (1998) uses the term to mean the metallicity of the progenitor star, while Lentz et al. (2000) uses it to mean the metallicity of the ejecta.

The differing definitions of metallicity yield different initial conditions, which resulted in contradictory results from these studies. Höflich et al. (1998) suggest that with increasing metallicity, the ultraviolet (UV) continuum of the SN increases, while Lentz et al. (2000) suggest that it decreases. Ultimately, the differences are the result of differing density structures (Lentz et al. 2000; Domínguez et al. 2001). Although the method of Lentz et al. (2000) seems less physical than that of Höflich et al. (1998) (simply scaling the metallicity of the ejecta by solar abundances does not take into account, for example, that the Fe-group elements are mainly produced in the SN explosion), they provide model spectra for varying metallicities, which may elucidate differences between low and high-redshift SN spectra.

Further predictions for lower metallicity include faster rise times (Höflich et al. 1998), faster light-curve decline (Höflich et al. 1998), lower  $^{54}\text{Fe}$  production (Höflich et al. 1998), smaller blueshifting of Si II  $\lambda 6355$  (Lentz et al. 2000), decreasing  $B - V$  color (Domínguez et al. 2001; Podsiadlowski et al. 2006), and changing luminosity (Höflich et al. 1998; Domínguez et al. 2001; Podsiadlowski et al. 2006; Timmes et al. 2003). Röpke & Hillebrandt (2004) suggest that the C/O ratio of the progenitor does not significantly affect peak luminosity.

Observationally, a lack of evolution has been supported by investigating various SN quantities such as rise time (Riess et al. 1999a), line velocities (Blondin et al. 2006; Garavini et al. 2007), multi-epoch temporal evolution (Foley et al. 2005), line strengths (Garavini et al. 2007), and line-strength ratios (Altavilla et al. 2006). There have also been studies comparing the spectra of individual high-redshift SNe Ia to low-redshift SNe Ia (Riess et al. 1998; Coil et al. 2000; Hook et al. 2005; Matheson et al. 2005; Balland et al. 2007), all of which have concluded that there is no clear difference in spectral properties between the two samples.

Bronder et al. (2007) recently presented measurements of line strengths that suggest a difference between low and high-redshift SNe Ia in one of three features measured. They find that the difference is highly dependent on the galaxy contamination at high redshift and might be affected by their small low-redshift SN sample. Consequently, they note that the difference is interesting but not significant.

Despite the consistencies in spectral properties,

Howell et al. (2007) note a slight shift in the mean photometric properties of SNe Ia with redshift. They explain this evolution as a change in the ratio of progenitors from the “prompt” and “delayed” channels (Scannapieco & Bildsten 2005), corresponding to young and old progenitor systems at the time of explosion, respectively. In particular, the light-curve shape parameter “stretch” (Goldhaber et al. 2001) increases with redshift. *HST* observations of ESSENCE objects suggested that the sample may have a large proportion of objects with slow-declining (large stretch) light curves, but this is probably the result of a selection bias (Krisciunas et al. 2005). Since stretch (and other luminosity light-curve parameters) is correlated with spectral properties, one might expect the spectra of high-redshift SNe Ia, on average, to differ from those of low-redshift SNe Ia.

Since all galactic environments at redshift  $0 < z < 1.5$  are also present in the local Universe, SN Ia evolution does not necessarily mean that there are not local analogs. For instance, if the distribution of observables is on average different at high redshift, as long as for each high-redshift SN there is a similar low-redshift counterpart, the peak brightness could, in principle, be correctly translated into an accurate distance. Within the local sample, there is no indication of a correlation between host-galaxy metallicity and light-curve shape (Gallagher et al. 2005).

In the process of classifying and finding the redshifts for SNe from the ESSENCE (Equation of State: Super-Novae trace Cosmic Expansion) survey (Miknaitis et al. 2007; Wood-Vasey et al. 2007), we have obtained 107 spectra which have accurate light-curve parameters such as  $\Delta$  (a light-curve width parameter), time of maximum light, and visual extinction (Matheson et al. 2005; Foley et al. 2008b). Most spectra in this sample have low signal-to-noise ratios (S/N) compared to spectra of low-redshift SNe. This makes impractical a detailed analysis of each object individually to test for outliers. However, by combining the spectra to make composite spectra, we are able to study the mean spectral properties of the samples.

In Section 2 we discuss our low and high-redshift SN Ia spectral samples. We describe our methods of creating composite spectra in Section 3. In Section 4 we present the composite spectra and compare the two samples, while in Section 5 we discuss the implications of these results. We present our conclusions in Section 6. Throughout this paper we assume the standard cosmological model with  $(h, \Omega_m, \Omega_\Lambda) = (0.7, 0.3, 0.7)$ .

## 2. SUPERNOVA SAMPLES

In order to test for potential evolution in SN Ia spectra, we need to explore the largest redshift range possible. Riess et al. (2007) have obtained spectra of 10 objects with  $z > 1$ , with one SN Ia at  $z = 1.39$ . The large look-back time of these objects allows significant time for progenitors to evolve between  $z \approx 1$  and  $z = 0$ ; however, even at  $z > 1$ , many galaxies had already become metal rich (e.g., Cimatti et al. 2004).

In addition to these high-redshift SN spectra, through the first four years of the ESSENCE campaign we have obtained 107 spectra of 88 SNe Ia with light curves that could be fit by MLCS2k2 (Jha et al. 2007). The spectra were obtained by the Keck I and II 10 m telescopes, the

Very Large Telescope (VLT) 8 m, the Gemini North and South 8 m telescopes, the Magellan Baade and Clay 6.5 m telescopes, the MMT 6.5 m telescope, and the Tillinghast 1.5 m telescope at the F. L. Whipple Observatory. The spectra are analyzed individually by Matheson et al. (2005) and Foley et al. (2008b), while the light curves are presented by Miknaitis et al. (2007). The spectra are in the redshift range of  $0.155 \leq z \leq 0.777$ , with corresponding rest-frame phases of  $-10.8 \leq t \leq 20.9$  d relative to  $B$ -band maximum. The objects span a wide range of light-curve width from  $-0.601 \leq \Delta \leq 0.843$ , corresponding to luminosities of  $-19.7 \leq M_V \leq -18.6$  mag at maximum brightness, respectively.

The observed wavelength ranges for the objects vary because the spectra were obtained with different instruments and each spectrum has been trimmed individually to remove the noisy ends of the spectrum. The rest-wavelength ranges are even more disparate because of the significantly different redshifts. The rest-frame spectra span the wavelength range 1940–8174 Å.

For the purpose of comparison, we have also composed a sample of 397 spectra obtained mainly with the Kast double spectrograph (Miller & Stone 1993) on the Lick 3-m telescope (Foley et al. 2008a), and 45 from *HST*/*IUE* (to sample the UV portion of the spectrum; SNe 1980N, 1981B, 1982B, 1983G, 1986G, 1989B Panagia 2007, 1990N, 1991T, Jeffery et al. 1992, 1992A Kirshner et al. 1993, 2001eh, and 2001ep Sauer et al. 2008). The light curves of these objects are presented elsewhere (Buta et al. 1985; Younger & van den Bergh 1985; Ciatti et al. 1988; Hamuy et al. 1996; Riess et al. 1999b; Jha et al. 2006; Ganeshalingam et al. 2008). The Lick objects are observed and reduced in a manner similar to the ESSENCE objects (Matheson et al. 2001, 2005; Foley et al. 2008b). These similarities reduce the systematic differences between observing programs. Although the *HST*/*IUE* spectra are not necessarily free of reduction errors, the differences should be minor and these spectra have great utility in our study.

In Figures 1, 2, and 3, we present histograms showing the  $\Delta$ , phase, and redshift distributions, respectively. The ESSENCE and Lick samples have similar distributions, and more importantly, the Lick spectra sample the entire range of phases and almost the entire  $\Delta$  range of the ESSENCE sample, allowing for an unbiased comparison. The total numbers of spectra in various redshift, phase, and  $\Delta$  bins are presented in Tables 1 and 2. All composite spectra presented in this paper are publicly available<sup>21</sup>.

### 3. METHOD

#### 3.1. Reprocessing

To properly combine our sample of SN spectra, we must first attempt to remove any effects of non-SN sources from each spectrum. The two main effects are reddening by host-galaxy dust and galaxy-light contamination.

The reddening of the spectra causes the spectral shape and relative feature strengths to change. To correct for the distortion introduced by reddening, we have used the MLCS reddening parameters listed in Table 5 and a standard reddening law (Cardelli et al. 1989) to deredden

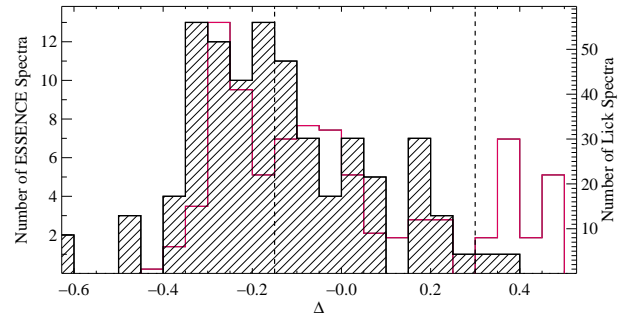


FIG. 1.— A histogram of the number of spectra per  $\Delta$  bin. The thick line with shading represents the ESSENCE objects, while the thin line represents the Lick objects. The dotted lines represent the distinction between the luminosity subclasses of SNe Ia (over-luminous, normal, and under-luminous correspond to  $\Delta < -0.15$ ,  $-0.15 < \Delta < 0.3$ , and  $\Delta > 0.3$ , respectively) from Jha et al. (2006).

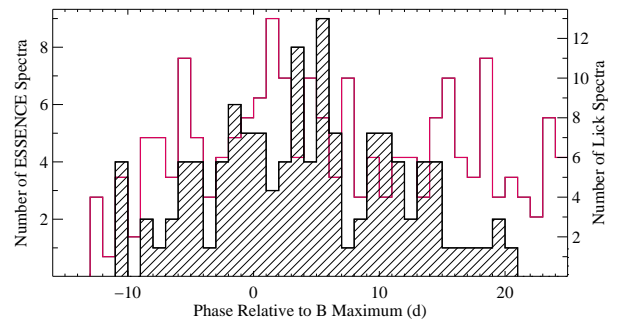


FIG. 2.— A histogram of the number of spectra per phase bin relative to the  $B$ -band maximum. The thick line with shading represents the ESSENCE objects, while the thin line represents the Lick objects.

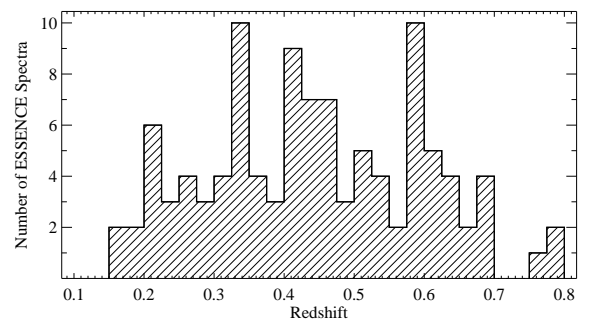


FIG. 3.— A histogram of the number of ESSENCE spectra per redshift bin.

our spectra. Since the ESSENCE photometry consists of only two bands, it is not possible to independently determine both  $A_V$  and  $R_V$ . To that extent, our corrected spectra may not be properly dereddened. The relative flux difference between a spectrum with  $A_V = 0.3$  mag with  $R_V = 2.1$  and  $R_V = 3.1$  is less than 10% for wavelengths longer than 3400 Å, and it is possible that the reddening parameters account for some intrinsic color variability within the SN sample (Conley et al. 2007). However, we have performed our analysis with both a low-extinction sample ( $A_V < 0.3$  mag) and our complete, treated sample (see Section 4.3), yielding similar results. Therefore, the errors in  $A_V$  and  $R_V$  are not

<sup>21</sup> <http://astro.berkeley.edu/~simrfoley/composite/>

TABLE 1  
NUMBER OF SPECTRA FOR REDSHIFT/PHASE BINNING

Redshift	$11 < t < -3$ d	$-3 < t < 3$ d	$3 < t < 10$ d	$10 < t < 17$ d	$17 < t < 23$ d
0	53	55	50	46	35
0 – 0.2	0	2	0	2	0
0.2 – 0.4	7	10	10	8	3
0.4 – 0.6	10	8	16	9	2
0.6 – 0.8	1	7	8	2	0

TABLE 2  
NUMBER OF SPECTRA FOR REDSHIFT/ $\Delta$  BINNING

Redshift	$\Delta < -0.15$	$-0.15 < \Delta < 0.3$	$\Delta > 0.3$
0	141	158	89
0 – 0.2	2	2	0
0.2 – 0.4	15	19	4
0.4 – 0.6	26	21	0
0.6 – 0.8	15	3	0

dominant.

At high redshift, the size of the SN host galaxy and the average offset between the host galaxy and the SN are small relative to the slits of our spectrographs. Consequently, it is often difficult to completely remove the galaxy-light contribution from the total light at the position of the SN. For some ESSENCE spectra, we employ a deconvolution technique (Blondin et al. 2005), which separates the SN and galaxy light better than simple background subtraction. With several bands of photometry for the galaxy, one can properly model the galaxy type, allowing one to find a matching template spectrum to subtract off the SN spectrum (Howell et al. 2005). However, using ESSENCE’s current photometry this is not possible. A campaign in underway to image the ESSENCE fields in *BVz*, and the resulting data should allow one to properly model the galaxy spectral-energy distribution (SED).

Obtaining a spectrum of the host galaxy after the SN has faded and subtracting an appropriate percentage of the host-galaxy spectrum from the SN spectrum is the best method to remove host-galaxy light contamination. This method, however, is typically very time intensive, and has not been performed on our sample. We have a program underway to obtain the host-galaxy spectra; however, observations have not yet begun. In this paper, we neglect the galaxy-light contamination in our spectra when making the composite spectra and then choose to compare our samples in a way that accounts for it (see Section 4).

### 3.2. Construction of the Composite Spectra

The composite spectra were constructed by first dereddening the individual spectra to the rest frame. The redshifts have errors up to 0.01 which might artificially widen some spectral features in the composite spectrum. If we wish to look at a dereddened spectrum, we then deredden the spectra based on our values of  $A_V$  and  $R_V$  found from fitting templates to the light curves ( $R_V$  is fixed at 3.1 for all ESSENCE objects, and unless the fits require  $R_V \neq 3.1$ , the low-redshift objects also have  $R_V$  fixed to 3.1; Jha et al. 2007). We then put the spectra through a low-pass filter to remove residual night-sky

lines, cosmic rays, and host-galaxy absorption and emission lines. By comparing the original spectra to a heavily smoothed version of each spectrum, we then determine the pixel-by-pixel S/N. Finally, we average the spectra, weighting by S/N. Since not all spectra have a common wavelength range (particularly comparing the *IUE* spectra to the Lick spectra), we first constructed a composite spectrum from the majority of spectra with overlapping wavelengths, and then used that temporary composite spectrum (which overlapped with all spectra) to match the fluxes of the individual spectra.

There are some intrinsic issues to constructing a composite SN spectrum. Despite having hundreds of SN spectra, to ensure a sufficient number of spectra per parameter bin we must still have somewhat large bins for some parameters such as phase. This can smear out certain features. However, since SN spectra tend to evolve smoothly over small time periods, averaging over a phase bin is a reasonable estimate for the average phase spectrum. Other issues are intrinsic differences in SN spectra. For a given phase and  $\Delta$ , spectra still differ from one object to another (Matheson et al. 2007). Or, within a particular bin, objects can have significantly different expansion velocities or colors. When constructing a composite spectrum, most of these spectral differences do not change the composite spectrum from looking like the “true” average SN spectrum. However, differences in expansion velocity will tend to make spectral features wider and shallower. Since we are comparing composite spectra to each other and not a composite spectrum to an individual spectrum, as long as the underlying samples are similar, the effects of differing expansion velocities will not create significant differences in the composite spectra.

The ESSENCE SNe come from a blind search, resulting in many objects in low-luminosity host galaxies. The Lick sample, on the other hand, comes primarily from targeted searches and is biased to higher-luminosity host galaxies. This may result in slightly different samples, however the similar  $\Delta$  distributions for the ESSENCE and Lick samples suggest against this. However, in creating composite spectra, since the spectra are weighted by S/N, the composite spectra will be weighted more towards intrinsically overluminous SNe Ia. Since this effect occurs in both samples, this should not affect our analysis.

### 3.3. Determining Spectral Variance

We want to determine both the average spectrum of a given phase,  $\Delta$ , and redshift, as well as the variation about that average spectrum. To do this, we implement a boot-strap sampling (with replacement) algorithm to estimate the variance (Efron 1982). The variance is a

combination of the noise in our spectra, any systematic effects during the reduction process (such as poor sky-line removal and incomplete galaxy-light subtraction), and the inherent variance in the SN sample.

For the Lick sample, the spectra are generally of very high quality with little noise or systematic issues. As such, the variance in these spectra is dominated by the intrinsic scatter among the objects. A detailed analysis of these spectra will be presented in a future paper (for another low-redshift composite spectrum derived from eight objects, see James et al. 2006). For the ESSENCE sample, the Poisson noise dominates at the bluest wavelengths since there are fewer spectra adding to the composite in this wavelength region and the spectra have lower S/N in the UV. The reddest wavelengths are dominated by reduction issues, specifically poor sky subtraction residuals. The observed wavelengths corresponding to night-sky lines are weighted less, but the average noise over large wavelength ranges remains higher at observed near-IR wavelengths than at visual wavelengths. The other major factor at long wavelengths is the large variation in host-galaxy contamination. Since the SEDs will vary dramatically based on the amount of galaxy-light contamination (SNe Ia are blue relative to galaxies), there is additional variance unrelated to the intrinsic variability of SN spectra.

#### 4. RESULTS

##### 4.1. Comparison of Low-Redshift Templates

To understand the subtle differences between the ESSENCE and low-redshift composite spectra, we must first examine the differences between different low-redshift composite spectra.

The original Nugent template spectra (Nugent et al. 2002) were constructed from 84 spectra (31 for the maximum-light template) of which 63% (52% near maximum light) come from SNe 1989B, 1992A, and 1994D. Two of these objects have been considered slightly atypical SNe Ia, with strong dust absorption (SN 1989B; Wells et al. 1994) or anomalous luminosity and colors (SN 1994D; Richmond et al. 1995; Patat et al. 1996). Since no SN is the perfect example of a SN Ia, the presence of these objects in the composite is not worrisome. However, having the majority of the sample rely on a few objects can severely skew the composite away from a true average. The Nugent templates have since been updated<sup>22</sup>, with more objects. However, the influence of these atypical SNe Ia is still strong.

A new spectral template has been constructed by Hsiao et al. (2007) for the Supernova Legacy Survey (SNLS). This template is created by combining low and high-redshift spectroscopy and photometry. It is created from a more varied sample than the Nugent template, but still has a very limited low-redshift sample.

The Lick maximum-light composite spectrum, the Nugent maximum-light template spectrum, and the new SNLS template spectrum are shown in Figure 4. The Nugent template is bluer at this phase, particularly in the UV and the near-UV. If normalized at 4000 Å, the Lick composite spectrum has higher flux levels than either the SNLS or Nugent template for wavelengths somewhat redder than 4300 Å, although it is very similar to

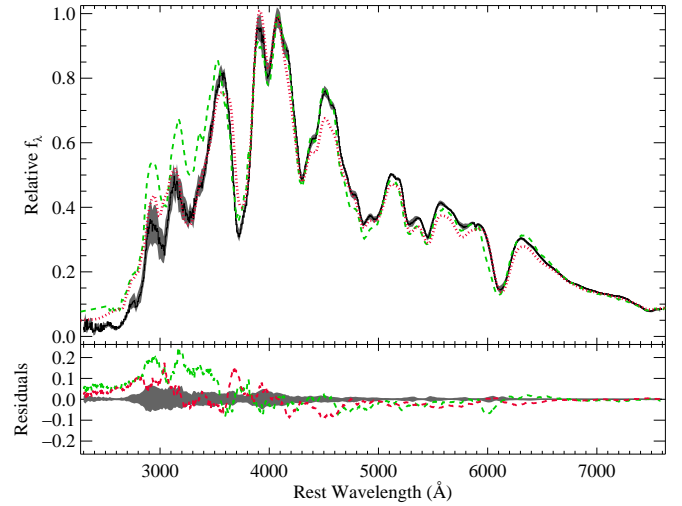


FIG. 4.— (*top panel*): Composite low- $z$  maximum-light SN Ia spectra. The black curve is the composite spectrum of the Lick sample; the green (dashed) curve is the Nugent template spectrum; and the red (dotted) curve is the SNLS template spectrum. The grey region is the  $1\sigma$  boot-strap variation of the Lick composite spectrum. (*bottom panel*): The difference between the Lick composite spectrum and the Nugent and SNLS template spectra. The grey region is the  $1\sigma$  boot-strap variation of the Lick composite spectrum.

the Nugent template in this region and to both templates for wavelengths redder than 4700 Å. Besides the feature at 4500 Å, the SNLS template is very similar to the Lick composite.

The only other region with major differences is in the UV (where the Nugent template also deviates from the Lick composite spectrum). Both the Nugent and SNLS templates are constructed by warping the spectra to match the colors of a normal SN Ia at the phase of the spectrum (for the SNLS template, this is done by using light-curve information in the construction of the template). However, the large dispersion in the  $U$  band (Jha et al. 2006) along with extrapolation into the UV makes the Nugent template UV continuum dubious. The Lick spectra were all observed and reduced in a consistent manner, producing relative spectrophotometry accurate to  $\sim \pm 5\%$  (Matheson et al. 2000). The colors for the three spectra as well as the colors of the MLCS  $\Delta = 0$  template light curves are presented in Table 3.

Considering the relative diversity of the Lick and Nugent samples and the methods of producing the composite spectra, we consider the Lick composite spectrum to be more reliable than the Nugent template. The SNLS template uses high-redshift SN data (both light curves and spectra) in the construction of their template. As a result, this template should not be used for comparison to high-redshift SNe Ia. In particular, the UV portion of the SNLS template is heavily weighted to high-redshift SNe Ia. Most importantly, the spectra in the Lick and ESSENCE samples were reduced and the composite spectra were constructed in the same manner. For our purposes, the Lick composite spectrum is superior to the alternatives and will be used for comparison in the rest of this paper.

The relative strengths of most absorption lines in the Nugent, SNLS, and Lick spectra are similar. The line velocities are also similar, with the exception of Si II 6355, which has a blueshift at maximum light of  $-12,300$

<sup>22</sup> [http://supernova.lbl.gov/~nugent/nugent\\_templates.html](http://supernova.lbl.gov/~nugent/nugent_templates.html).



TABLE 3  
LOW-REDSHIFT MAXIMUM-LIGHT COLORS

Spectrum	$U - B$ (mag)	$B - V$ (mag)	$V - R$ (mag)	$V - I$ (mag)
MLCS $\Delta = 0$	-0.47	-0.07	0.00	-0.29
Lick	-0.33	-0.04	-0.04	-0.34
Nugent	-0.45	-0.07	0.00	-0.35
SNLS	-0.41	-0.06	-0.02	-0.26

$\text{km s}^{-1}$  (Nugent template) versus  $-11,200 \text{ km s}^{-1}$  (SNLS template) and  $-11,400 \text{ km s}^{-1}$  (Lick composite). Another interesting difference is the weaker feature at  $\sim 3000 \text{ \AA}$  in the SNLS template compared to the Nugent template and Lick composite spectrum. Although Hsiao et al. (2007) show no major difference at this wavelength when including or excluding high-redshift spectra, the final SNLS template contains both high-redshift spectra and light-curve information, which may result in a bias for the  $\sim 3000 \text{ \AA}$  feature (see Section 5.2).

#### 4.2. Maximum-Light Spectrum

The nature of the ESSENCE search dictates that most objects are observed spectroscopically near maximum light. As seen in Figure 2, most spectra were obtained near maximum light (64/107 have rest-frame phases within one week of maximum light), with a median of 4.1 d after maximum light. Since objects are brightest at maximum light, the highest S/N spectra are usually obtained at this phase and the contrast between the SN and the underlying galaxy is largest. These factors together make the maximum-light composite spectrum a higher S/N spectrum.

In Figure 5, we present the ESSENCE maximum-light composite spectrum with average parameters  $\langle z \rangle = 0.37$ ,  $\langle t \rangle = -0.8 \text{ d}$ , and  $\langle \Delta \rangle = 0.01$ . Comparing the spectrum to the Lick maximum-light spectrum (which has average parameters  $\langle z \rangle = 0.02$ ,  $\langle t \rangle = 0.5 \text{ d}$ , and  $\langle \Delta \rangle = -0.02$ ), it is obvious that the two spectra have rather different colors, with the ESSENCE spectrum being redder than the Lick spectrum.

As described in Section 4.4, the large projected size of the slit for high-redshift objects makes isolating the SN from the host galaxy difficult. It is much easier to separate the SN from the galaxy light at low redshift. Our ability to remove host-galaxy light from any given SN spectrum hinges on how well we can model the galaxy background, which is highly dependent on how isolated the SN is from its host galaxy. To account for the difference in the amount of galaxy light remaining in a SN spectrum, we fit a combination of a galaxy spectrum and the Lick composite spectrum to match the ESSENCE spectrum. Similar to the method of (Howell et al. 2005), using five galaxy spectra templates (E, S0, Sa, Sb, and Sc) and varying the galaxy light from 0% to 100% of the comparison spectrum, we find a best-fit combination. As seen in Figure 5, by adding some galaxy light (35% of an Sb galaxy spectrum for the maximum-light spectrum) to the Lick spectrum, we can match the Lick and ESSENCE spectra quite well. We believe galaxy-light contamination to be the main factor in the discrepancy between the Lick and ESSENCE continua.

Properly determining the galaxy contamination is cru-

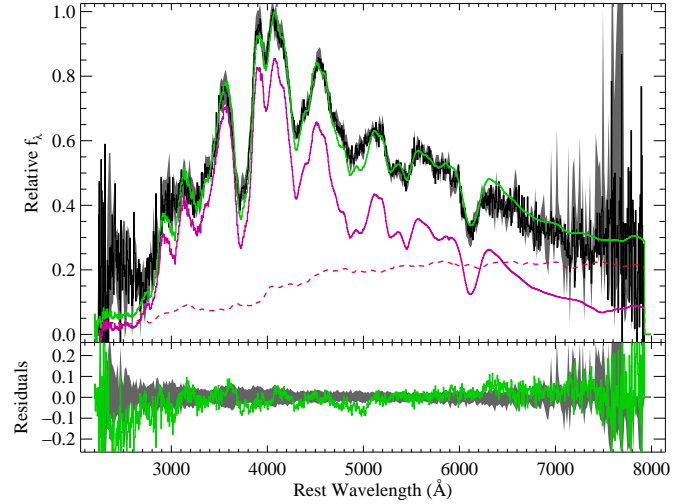


FIG. 5.— (*top panel*): ESSENCE maximum-light composite SN Ia spectrum. The black, relatively noisy curve is the ESSENCE composite spectrum. The purple curve, slightly below the black curve, is the Lick maximum-light composite spectrum. The red (dashed) curve is an Sb galaxy spectrum. The green curve is the addition of the red and purple curves, fit to match the ESSENCE composite spectrum. The combination is 35% of host-galaxy spectrum in the region 4000–6000 Å. The grey region is the  $1\sigma$  bootstrap variation of the ESSENCE composite spectrum. The large variance at red wavelengths is due to strong sky-subtraction residuals in individual spectra and not intrinsic variability in the SN sample. (*bottom panel*): The difference between the ESSENCE and Lick composite spectra. The grey region is the  $1\sigma$  bootstrap variation of the ESSENCE composite spectrum.

cial in determining differences between our two samples. We have performed several tests to determine the validity of our claims with different galaxy contamination.

In addition to fitting template galaxy spectra to our observed spectra, we have reconstructed the best-fit galaxy spectra from galaxy eigenspectra. Using the first four Sloan Digital Sky Survey (SDSS) galaxy eigenspectra (Yip et al. 2004), we fit the eigenspectra to the residuals of the ESSENCE and Lick spectra. Higher-order eigenspectra are dominated by emission lines and high-frequency modulations.

The process consists of reducing the  $\chi^2$  of

$$f_{\text{ESSENCE}} - (af_{\text{Lick}} + \mathbf{b}\mathbf{U}_{\text{SDSS}}^t), \quad (1)$$

where  $f_{\text{ESSENCE}}$  is the flux vector of the ESSENCE composite spectrum,  $f_{\text{Lick}}$  is the flux vector of the Lick composite spectrum,  $\mathbf{U}_{\text{SDSS}} = \{e_i\}$ ,  $1 \leq i \leq 4$  is the matrix of SDSS eigenspectra,  $a$  is a free parameter, and  $\mathbf{b}$  is the eigenvector that best describes the  $f_{\text{ESSENCE}} - af_{\text{Lick}}$  residual. The best-fit reconstructed galaxy spectrum is comprised of 83.5%, 7.2%, 5.6%, and 3.7% of the first-four eigenspectra, respectively. The first eigenspectrum is the average of the SDSS galaxy sample and resembles an Sb galaxy.

In Figure 6, we present the principal-components analysis (PCA) reconstructed best fit, and our Sb galaxy template spectrum. The PCA-reconstructed and template spectra are fit with differing amounts of SN light, so their absolute scaling is approximately the same, but slightly different. Despite this, we can still see that the PCA and Sb template spectra have very similar SEDs, differing the most around 4200 Å and at wavelengths longer than 6500 Å. Extrapolating the PCA spectrum, it appears that the spectra do not differ drastically in the

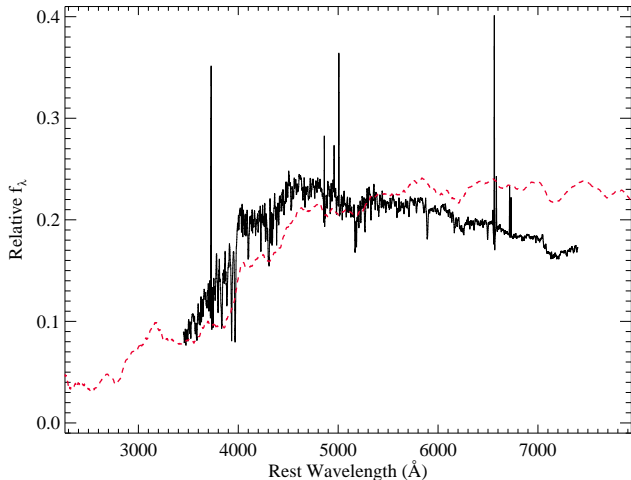


FIG. 6.— The best-fit PCA-reconstructed and template galaxy spectra (black and red curves, respectively). Since the amount of galaxy light in the fit changes based on the SED of the galaxy spectrum, the scaling between the spectra is arbitrary.

UV.

Figure 7 shows the fit and residuals of the PCA-reconstructed galaxy spectrum (similar to Figure 5). The residuals for the PCA-reconstructed fit are smaller than those for the template fit. Since the addition of the PCA-reconstructed galaxy spectrum to the Lick composite spectrum gives, by construction, the smallest deviation from the ESSENCE composite spectrum, we consider any additional differences to come from sources other than galaxy contamination. Considering the overall similar results and smaller wavelength range of the PCA-reconstructed galaxy spectrum, we will use the template galaxy spectrum for comparisons, but note differences with the PCA-reconstructed galaxy spectrum when appropriate.

It is unlikely that miscalculated reddening corrections can cause the differences in the continua. Using the unreddened sample of spectra produces a similar continuum (see Section 4.3). Although it is possible that SN evolution could cause the discrepancy, no current models predict that the spectrum would change in this way.

After correcting for galaxy-light contamination, by adding galaxy light to the Lick composite spectrum<sup>23</sup>, the Lick spectrum is very similar to the ESSENCE composite spectrum. Despite the similarities, there are two differences worth noting: the ESSENCE composite spectrum lacks the absorption at  $\sim 3000$  Å and has a weaker feature at  $\sim 4900$  Å. The feature at  $\sim 3000$  Å is attributed to multiple Fe II lines (Branch & Venkatakrishna 1986), while the feature at  $\sim 4900$  Å is attributed to Si II, Fe II, and Fe III, with the red wing, where the discrepancy occurs, being Fe III  $\lambda 5129$ . We will use the convention of Garavini et al. (2007) and call the entire feature “Fe II 4800,” naming the lines individually only when we are discussing particular species contributing to the feature.

Using the prescription of Garavini et al. (2007), we measure the pseudo-equivalent widths (pEWs) of several

<sup>23</sup> Throughout this paper, in all comparisons, ESSENCE composite spectra are presented unchanged, and Lick composite spectra have additional galaxy light to match the ESSENCE spectra, unless specifically noted.

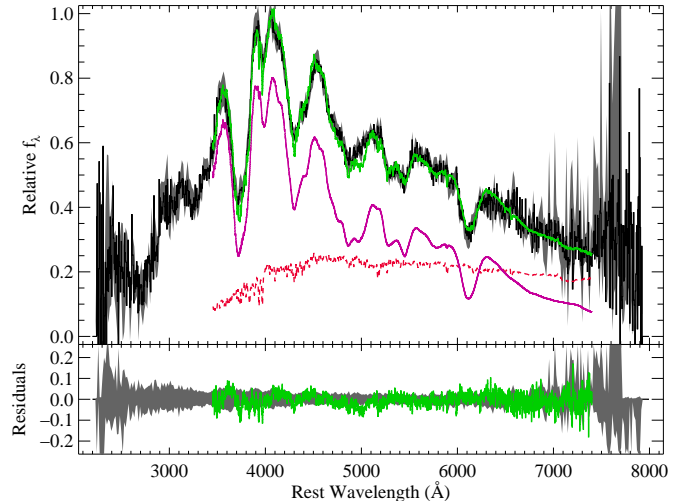


FIG. 7.— (*top panel*): ESSENCE maximum-light composite SN Ia spectrum. The black, relatively noisy curve is the ESSENCE composite spectrum. The purple curve, slightly below the black curve, is the Lick maximum-light composite spectrum. The red (dashed) curve is the sigma-clipped SDSS PCA-reconstructed galaxy spectrum. The green curve is the addition of the red and purple curves, fit to match the ESSENCE composite spectrum. The combination is 40% of galaxy spectrum in the region 4000–6000 Å. The grey region is the  $1\sigma$  boot-strap variation of the ESSENCE composite spectrum. The large variance at red wavelengths is due to strong sky-subtraction residuals in individual spectra and not to intrinsic variability in the SN sample. (*bottom panel*): The difference between the ESSENCE and Lick composite spectra. The grey region is the  $1\sigma$  boot-strap variation of the ESSENCE composite spectrum.

features in both the ESSENCE and Lick composite spectra. These values are presented in Table 4. We note that because of the host-galaxy contamination, the pEWs of the ESSENCE composite spectrum are lower limits. We have calculated the pEWs of the Lick composite spectrum both with and without galaxy light added. The values of the spectrum with galaxy light added should be compared directly to the values of the ESSENCE spectrum; however, the values without galaxy light give both an accurate measurement and an upper limit for the pEWs. There is significant systematic uncertainty to these measurements from the placement of the continuum. We did not attempt to model the exact systematic errors, but they are typically  $\sim 10$  Å (Garavini et al. 2007).

For most features, the ESSENCE and Lick composite spectra have similar pEWs. Bronder et al. (2007) found a possible difference in the strength of the Mg II 4300 feature, but we see no difference in our composite spectra. We will show a full analysis similar to the Bronder et al. (2007) study in Foley et al. (2008b). The Si II 6150 pEW has a slightly smaller value in the ESSENCE spectrum. Similarly, the Fe II 4800 feature is much weaker in the ESSENCE spectrum, which is likely because of a weaker Fe III  $\lambda 5129$  line. Using the PCA-reconstructed galaxy spectrum, we see that the Lick Si II feature has a similar pEW to the ESSENCE composite spectrum. The Fe II 4800 feature continues to have a larger (although slightly smaller than using the galaxy template spectrum,  $\text{pEW} = 94.9 \pm 0.2$  Å) pEW than the ESSENCE composite spectrum. The PCA-reconstructed galaxy spectrum does not cover the 3000 Å region.

TABLE 4  
PSEUDO-EQUIVALENT WIDTHS

Spectrum	Ca II H&K (Å)	Si II 4000 (Å)	Mg II 4300 (Å)	Fe II 4800 (Å)	S II W (Å)	Si II 6150 (Å)
Lick	112.8 (0.6)	12.4 (0.6)	86.4 (0.4)	140.9 (0.4)	68.5 (0.4)	99.5 (0.6)
Lick + Galaxy	100.7 (0.5)	9.6 (0.4)	73.6 (0.3)	98.8 (0.2)	43.4 (0.2)	61.4 (0.3)
ESSENCE	99.7 (1.1)	9.7 (0.5)	73.8 (0.8)	78.5 (0.8)	45.7 (0.8)	51.7 (1.7)

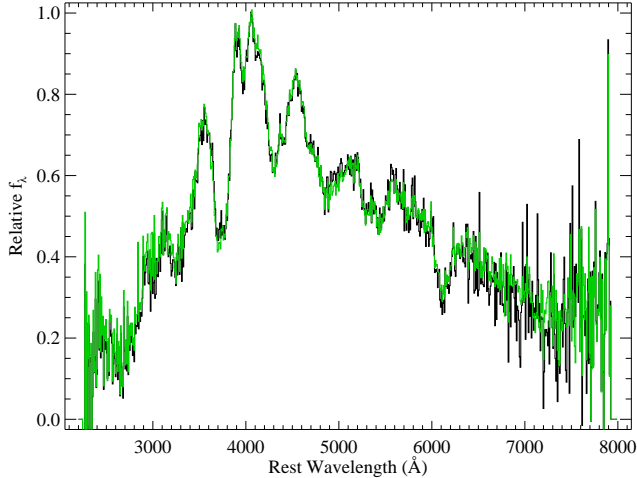


FIG. 8.— ESSENCE low- $A_V$  maximum-light composite SN Ia spectrum. The black curve is the ESSENCE low- $A_V$  composite spectrum and the green curve is the ESSENCE full-sample maximum-light composite spectrum (as shown in Figure 5). The spectra contributing to the full-sample spectrum have been dereddened by the values listed in Table 5. The low- $A_V$  spectrum has not been dereddened. The low- $A_V$  and full-sample spectra are nearly identical, indicating that the difference between the Lick and ESSENCE spectra is not the result of miscalculated reddening corrections.

#### 4.3. Low-Extinction Spectrum

As mentioned in Section 4.2, a possible explanation for the difference between the Lick and ESSENCE composite spectra is a miscalculation of the reddening from the light curves. To test this hypothesis, we have created an un-dereddened composite spectrum using only objects with  $A_V < 0.3$  mag. This subsample is less dependent on the precise values of  $A_V$  and  $R_V$ , reducing those potential sources of systematic error. Figure 8 shows both the full, dereddened and low- $A_V$  (with no dereddening) ESSENCE composite spectra. Both the low- $A_V$  and full, dereddened ESSENCE samples produce nearly identical spectra. There is a slight difference between the continua, with the low- $A_V$  sample being slightly redder. This is probably due to the slight extinction that has not been corrected in the contributing spectra.

#### 4.4. Redshift-Binned Spectra

We have divided the full sample of ESSENCE spectra into four redshift bins with  $\Delta z = 0.2$ . Since the ESSENCE sample is confined to  $z < 1$ , we also utilize the composite spectrum of Riess et al. (2007), which has  $\langle z \rangle = 1.1$ . The composite spectra with mean phases  $\langle t \rangle = -2.2, -0.6, -0.1$ , and  $-0.1$  d for the  $0 < z < 0.2$ ,  $0.2 < z < 0.4$ ,  $0.4 < z < 0.6$ , and  $0.6 < z < 0.8$  bins (respectively) are presented in Figure 9. Broadly, the spectra resemble each other with no major differences

except for redder continua with increasing redshift. We attribute the redder colors with increasing redshift to an increase in the galaxy fraction of the spectrum.

Using the method described in Section 4.2, we determined the galaxy-light fraction of each redshift-binned composite spectrum. Figure 10 shows the galaxy fraction of the redshift-binned ESSENCE composite spectra. For comparison, we also show the relationship between the projected distance of  $1''$  and redshift, given by

$$d_{\perp} = 4.848 \times d_L \left( \frac{\theta}{1''} \right) (1+z)^2 \text{ kpc}, \quad (2)$$

where  $d_L$  is the luminosity distance given in Gpc. If the separation between the SN and the galaxy is less than the larger of the slit width and the seeing, both typically  $1''$ , there will be galaxy contamination in the SN spectrum. If the galaxy is larger than the seeing, the separation can be larger and the SN spectrum can still be contaminated by galaxy light. If the physical distance between SN and galaxy nucleus, galaxy luminosity, and galaxy size do not change, either by galaxy evolution or selection effects, we expect the galaxy fraction to increase with  $d_{\perp}$  since larger redshift corresponds to more of the galaxy in the slit. Figure 10 shows this trend, further suggesting that the main difference between the Lick and ESSENCE composite spectra is the result of galaxy-light contamination. The *HST* composite spectrum is not affected by galaxy-light contamination since the high angular resolution and narrow slits of *HST* give comparable conditions to those of the low-redshift objects. Confirming this hypothesis, our galaxy-light fitting routine yields a best fit of 0% galaxy light for the *HST* composite spectrum.

In the three lowest-redshift bins, we are able to examine the Si II  $\lambda 6355$  line. In these bins, it does not appear to be stronger at higher redshift, consistent with that found for the maximum-light spectrum (see Section 4.2 and Table 4). The major differences between the total maximum-light composite ESSENCE spectrum and the Lick composite spectrum are the lack of absorption at  $\sim 3000$  Å in the ESSENCE spectrum and the weaker Fe III  $\lambda 5129$  line. Both lines are shown in detail in Figure 9. The  $\sim 3000$  Å line is only available in the three highest-redshift bins. In the  $0.2 < z < 0.4$  bin, there appears to be some absorption at this wavelength. The  $0.4 < z < 0.6$  bin does not appear to have any absorption, but the line does have a positive pEW that is  $3.3\sigma$  from zero. For the highest-redshift bin ( $z > 0.6$ ), the absorption is lacking. The Fe III  $\lambda 5129$  line is within the wavelength range of all ESSENCE redshift-binned composite spectra. The lowest two redshift bins appear to have line strengths consistent with the Lick composite spectrum. However, the highest two redshift bins appear to be lacking some absorption.

The UV portion of the Lick composite spectrum con-



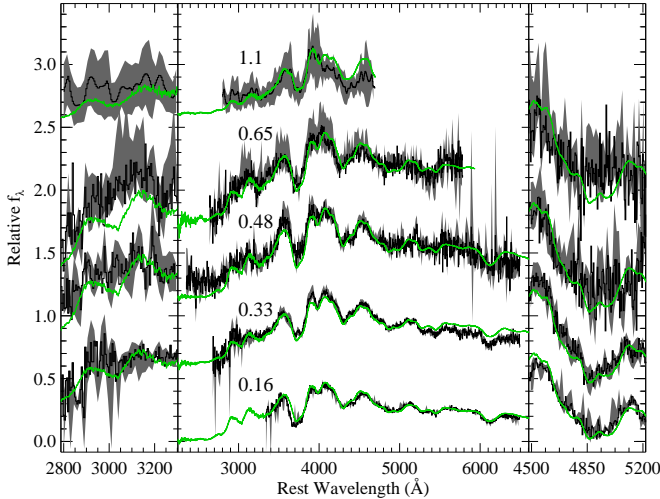


FIG. 9.— ESSENCE maximum-light composite SN Ia spectra for different redshift bins. The spectra have average redshifts of 0.16, 0.33, 0.48, and 0.64, as well as average phases of  $-2.2$  d,  $-0.6$  d,  $-0.1$  d, and  $-0.1$  d, respectively. The grey regions are the  $1\sigma$  boot-strap variation. The green curves are the Lick maximum-light composite spectrum with 34%, 35%, 41%, and 49% galaxy light for the comparisons to the  $\langle z \rangle = 0.16$ ,  $\langle z \rangle = 0.33$ ,  $\langle z \rangle = 0.48$ , and  $\langle z \rangle = 0.65$  bins, respectively. The *HST* composite spectrum from Riess et al. (2007), with  $\langle z \rangle = 1.1$ , is composed of individual spectra spanning phases of 0–10 d past maximum brightness. For comparison, a Lick composite spectrum was constructed from low-redshift spectra with similar phases. For the *HST* composite spectrum, no galaxy light was added to the Lick comparison spectrum. We argue that galaxy-light contamination should be lower in the *HST* spectra (see text), and this is confirmed by our galaxy-light fitting routine which gives a best fit with no galaxy light. The left and right panels show the regions surrounding the  $\sim 3000$  Å and Fe II 4800 features.

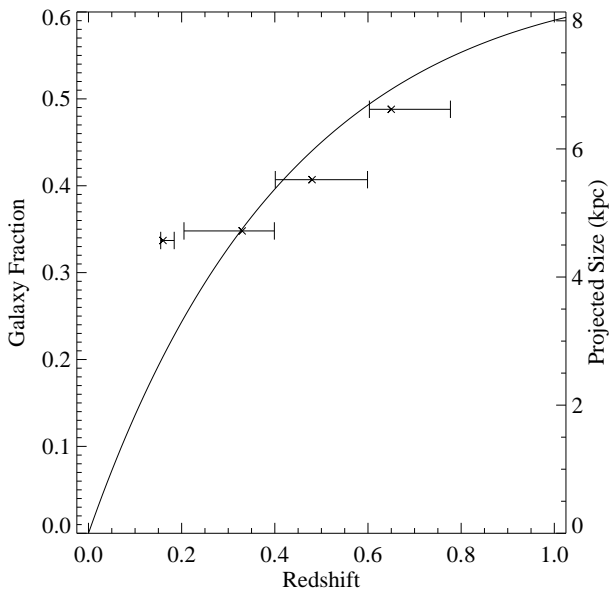


FIG. 10.— The galaxy fraction for ESSENCE maximum-light composite spectra of varying redshifts found by fitting the Lick maximum-light composite spectrum and a varying amount of galaxy light to the ESSENCE spectra. The solid curve represents the projected size of  $1''$  with redshift. The typical size of a slit used to obtain the spectra is  $1''$ .

sists of only a few spectra from even fewer objects. As such, the  $\sim 3000$  Å feature might be anomalous for typical SNe Ia. However, the presence of this line in one of our ESSENCE spectra but not in the two highest-redshift bins suggests that the line has some redshift dependence. Since we preferentially select objects that have bright UV fluxes at higher redshift, this may be a bias in the sample. The  $\langle z \rangle = 1.1$  composite spectrum from Riess et al. (2007) does show a slight dip at  $3000$  Å, but the spectrum is rather noisy at  $\lambda < 3500$  Å and the dip is narrow compared to other features, so it is likely insignificant. If the line is present in the *HST* spectrum but not in the highest-redshift bins of the ESSENCE sample, then it is likely associated with another property that changes with redshift in the ESSENCE sample, but is unaffected in the *HST* objects, presumably the result of a selection effect. Unfortunately, the *HST* composite spectrum does not contain the Fe III  $\lambda 5129$  feature, so we are unable to confirm the trend to higher redshifts and to determine if the trend is the result of a selection effect.

#### 4.5. Phase-Binned Spectra

Another subsampling we created was based on phase, as estimated from the light curves. We present five phase-binned composite spectra in Figure 11, corresponding to roughly one week before maximum light, maximum light, and one, two, and three weeks after maximum light, having phase bins of  $-11 < t < -3$  d ( $\langle t \rangle = -6.2$  d),  $-3 < t < 3$  d ( $\langle t \rangle = -0.8$  d),  $3 < t < 10$  d ( $\langle t \rangle = 5.6$  d),  $10 < t < 17$  d ( $\langle t \rangle = 13.3$  d), and  $17 < t < 23$  d ( $\langle t \rangle = 17.9$  d), respectively. Again, all ESSENCE composites are generally similar to the Lick composites with some differences.

The  $-6.2$  d ESSENCE spectrum displays three noteworthy differences: a higher Si II  $\lambda 6355$  velocity ( $12,800$  km s $^{-1}$  versus  $12,100$  km s $^{-1}$  for the Lick spectrum), a slightly stronger Si II  $\lambda 6355$  line, and a UV excess. The ESSENCE spectrum has a slightly older average phase ( $-6.2$  d compared to  $-6.6$  d) and slightly smaller average  $\Delta$  ( $-0.14$  compared to  $-0.08$ ). Although these differences are small, they may account for part of the different Si velocity and line strength. For some SNe, our redshift errors can be as large as  $\sim 3000$  km s $^{-1}$ , which is much larger than the difference between the two velocity measurements. However, the other lines in the spectrum, including the Si II  $\lambda 4130$  line, do not show this velocity shift, indicating that this is intrinsic to the Si II  $\lambda 6355$  line. The UV excess is very difficult to explain as merely a systematic error, although see Section 5.2 for a discussion of the possible issues regarding the treatment of the galaxy-light contamination.

The  $-0.8$  d maximum-light ESSENCE spectrum is discussed in Section 4.2.

The  $5.6$  d ESSENCE spectrum is similar to the comparable Lick spectrum, but there are more differences than in the earlier spectra. The blue wing of the Si II doublet ( $\lambda 5612$ ) is stronger and the overall continuum matching is worse than with other spectra. This is likely the result of poor galaxy-contamination correction. Later epoch spectra require starburst-galaxy spectra for the Lick spectra to match the continua of the ESSENCE spectra. The  $5.6$  d spectrum may be the transition between these two regimes.

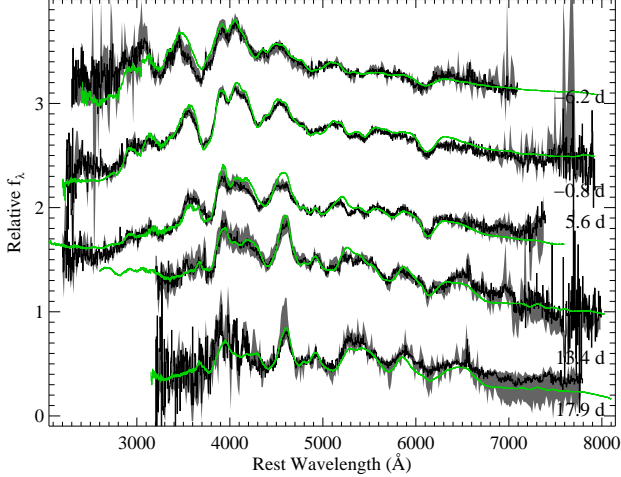


FIG. 11.— ESSENCE composite SN Ia spectra for different phase bins. The spectra have phase bins of  $-11 < t < 3$  d,  $-3 < t < 3$  d,  $3 < t < 10$  d,  $10 < t < 17$  d, and  $17 < t < 23$  d, with average phases of  $-6.2$  d,  $-0.7$  d,  $5.7$  d,  $13.3$  d, and  $17.9$  d, respectively. The  $-3 < t < 3$  d spectrum is the same as in Figure 5. The grey regions are the  $1\sigma$  boot-strap variation. The green lines are Lick composite spectra with the same phase bins and similar average phases.

The 13.3 d and 17.9 d ESSENCE spectra are also similar to their Lick counterparts. However, to make this match, it was necessary to include a percentage of starburst-galaxy spectra. Restricting our fitting method to normal galaxies, all features match between the ESSENCE and Lick spectra, but their strengths are very different, with the Lick features being much stronger. With only normal galaxy light, the ESSENCE spectra have very large blue excesses. Unfortunately, these bins contain lower-redshift SNe, and as such, we are unable to probe the UV portion of the spectrum.

#### 4.6. $\Delta$ -Binned Spectra

To test the possibility that a certain luminosity-based subsample may deviate from the local comparison, we separated the objects into three luminosity bins defined by Jha et al. (2006) of  $\Delta < -0.15$ ,  $-0.15 < \Delta < 0.3$ , and  $\Delta > 0.3$ , corresponding to overluminous, normal, and underluminous objects, respectively.

In Figure 12, we present the luminosity-binned maximum-light ESSENCE composite spectra as well as the total and luminosity-binned Lick spectra for comparison. The ESSENCE and Lick spectra are all generally consistent with both the total and luminosity-binned Lick spectra. The total and luminosity-binned spectra are similar, with the total and normal-luminosity spectra being nearly identical. This indicates that the total composite spectra of Lick (and to some degree the ESSENCE spectra) are a proxy for the normal-luminosity SNe Ia.

The normal-luminosity ESSENCE and Lick spectra are very similar, with the spectra having minor differences. The underluminous spectra are also very similar; the main difference is that the Si II  $\lambda 5972$  line is slightly stronger in the ESSENCE composite. Since the underluminous composite is constructed from only three spectra, this difference might not persist for a larger sample. Although the overluminous spectra are generally similar, there are minor differences between the Lick and ESSENCE composite spectra. The Fe II 4800 feature,

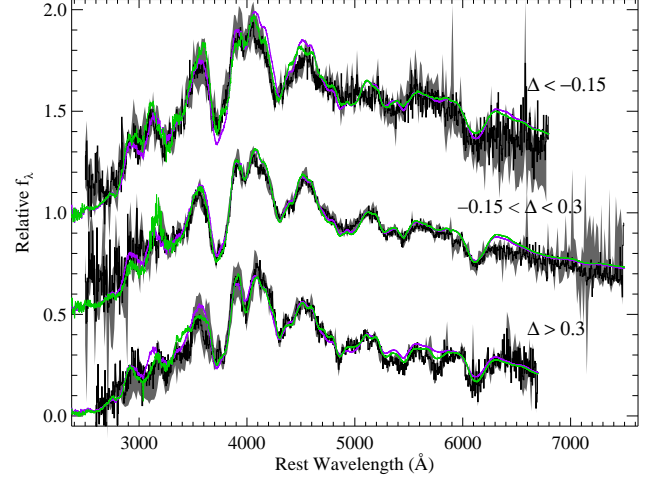


FIG. 12.— ESSENCE maximum-light composite SN Ia spectra for different  $\Delta$  bins. The composite spectra consist of 3 (10), 14 (18), and 15 (9) individual spectra with average  $\Delta$  of 0.33, (0.43), 0.01 ( $-0.05$ ), and  $-0.32$  ( $-0.28$ ) for the underluminous, normal, and overluminous subsamples defined by Jha et al. (2006) ( $\Delta > 0.3$ ,  $-0.15 < \Delta < 0.3$ , and  $\Delta < -0.15$ ) for the ESSENCE (Lick) sample, respectively. All have average redshifts of  $\sim 0.3$ . The grey regions are the  $1\sigma$  boot-strap variation. The green lines are the Lick composite comparison spectra.

which includes the Fe III  $\lambda 5129$  line, is weaker in the ESSENCE spectrum, practically vanishing.

## 5. DISCUSSION

Section 4 shows that in every instance, the overall appearance of the low-redshift Lick and high-redshift ESSENCE spectra is very similar, with only a few small but notable differences. In multiple cases, the Fe II absorption at  $\sim 3000$  Å present in the Lick composite spectra is missing in the ESSENCE composite spectra. Similarly, the Fe II 4800 feature is weaker in the ESSENCE spectra, particularly at higher redshift and smaller  $\Delta$  (that is, overluminous SNe Ia). The Si II  $\lambda 6355$  line is perhaps slightly stronger in the premaximum ESSENCE composite spectrum, but weaker in others. In the premaximum ESSENCE composite spectrum, there is a UV excess and the Si II  $\lambda 6355$  line is blueshifted more compared to the Lick composite spectrum. In this section, we attempt to explain the physical nature as well as some consequences of these differences.

### 5.1. Evolution vs. Changing Demographics

If there is a true spectroscopic difference between low and high-redshift SNe Ia, it is still necessary to determine if objects with the same value of  $\Delta$  (and hence the same light-curve shape, to first order) are changing with redshift (evolution) or if the population of the objects is changing with redshift (changing demographics). If, for instance, SNe with a given value of  $\Delta$  are changing with redshift as a result of metallicity differences, we would call that “evolution.” On the other hand, if the metallicity is lower in star-forming galaxies and more SNe Ia occur in star-forming galaxies at high redshift, causing the average SN to have lower metallicity, we would call that “changing demographics.”

A difference in samples caused by both changing demographics and evolution are possibilities. Photometric information suggests that SN Ia demographics do change

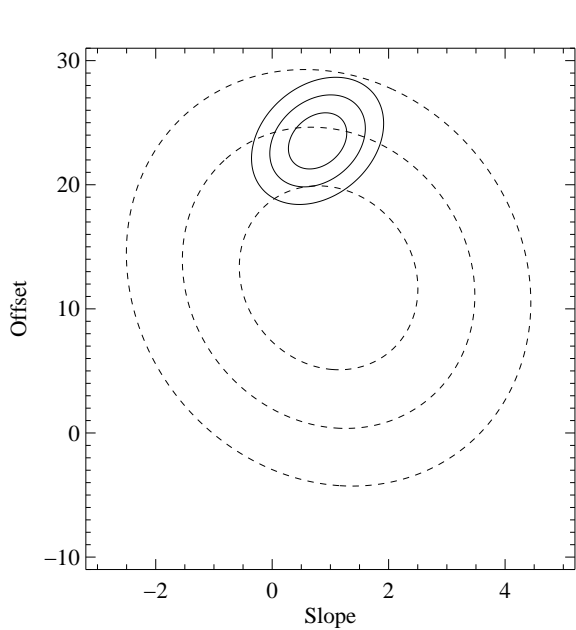


FIG. 13.—  $1\sigma$ ,  $2\sigma$ , and  $3\sigma$  confidence contours for the linear fit parameters for the  $\sim 3000$  Å feature. The smaller, solid contours are for the Lick sample. The larger, dashed contours are for the ESSENCE sample.

with redshift (Howell et al. 2007); namely there are more objects with higher stretch at high redshift. Until we compare objects with similar conditions (host galaxies, delay times, etc.), we will not be able to distinguish between these possibilities.

## 5.2. Line Strengths

### 5.2.1. Fe II 3000

The Fe II  $\sim 3000$  Å absorption is absent in the normal-luminosity ESSENCE composite spectrum, but the feature has similar strength in the overluminous ESSENCE and Lick composite spectra. Although the Fe II 4800 feature is also weaker at higher redshift (because of a weaker Fe III  $\lambda 5129$  line, which is a component of the Fe II 4800 feature), the opposite is true, with the line being weaker in the overluminous ESSENCE composite spectrum but having similar strength in the normal luminosity ESSENCE and Lick composite spectra. It is therefore unlikely that the lack of the Fe II  $\sim 3000$  Å absorption is the result of an ionization or density effect (although there may be non-LTE effects). Alternatively, there may be another species contributing to the feature.

To determine the significance of the differences in the strength of this feature, we measured the line in individual spectra. After adding the appropriate amount of galaxy light (measured from the fit to the spectra), we measured the pEW of all low-redshift spectra. We then fit a line to the pEWs as a function of age for  $-11 < t < 11$  d. We also performed a linear fit for the ESSENCE data over the same age range. In Figure 13, we show the confidence contours of the fit parameters for the Lick and ESSENCE samples. The contours overlap, indicating that the differences in the samples are not significant.

Nevertheless, we do see some indications of differences in the strength of the line with redshift. As seen in Figure 14, the Lick composite spectrum shows a strong line, while the  $z > 0.6$  ESSENCE and *HST* spectra show

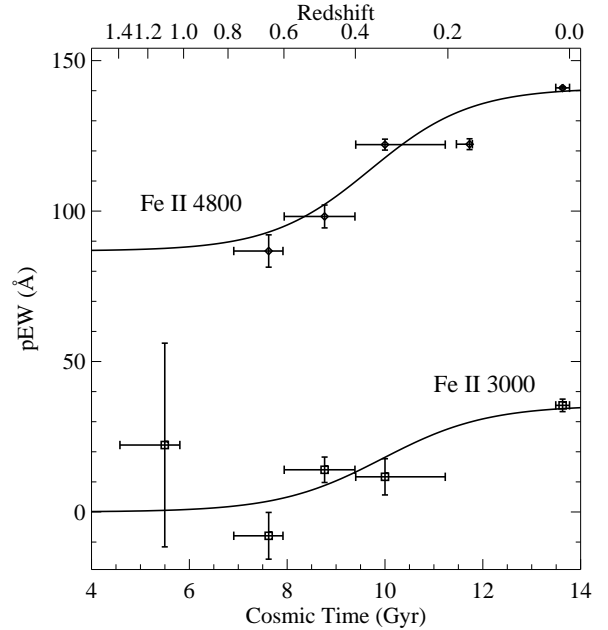


FIG. 14.— Pseudo-equivalent widths of the  $\sim 3000$  Å (squares) and Fe II 4800 (diamonds) features as a function of cosmic time. The highest-redshift bins are consistent with  $\text{pEW}(3000 \text{ Å}) = 0$ . Overplotted are the best-fit Verhulst (1845) curves showing a transition from weaker to stronger features at  $t_{tr,3000} = 9.9$  Gyr ( $z_{tr,3000} = 0.34$ ) and  $t_{tr,4800} = 9.7$  Gyr ( $z_{tr,4800} = 0.36$ ). The pEW errors shown are only statistical; systematic errors are typically 10 Å. The decrease in the Fe II 4800 feature may be artificially smaller at higher redshift. See Figure 16 for measurements of individual spectra.

no indication of a line. The lower-redshift ESSENCE composite spectra also show weaker lines. We note that visually, there appears to be a slight absorption in the  $\langle z \rangle = 0.33$  spectrum, but nothing distinct in the  $\langle z \rangle = 0.48$  spectrum. There may be absorption in the *HST* composite spectrum (see Section 4.4 and Figure 9), but it is consistent with no line. Considering the systematic uncertainties, it is possible that the data can be fit with a straight line and there is no change with redshift.

In Figure 14, we plot the evolution of pEW of the  $\sim 3000$  Å feature with cosmic time. Using a Verhulst (1845) function, which is a logistic function originally used to describe population growth, we fit the pEWs assuming  $\text{pEW}(t = 0) = 0$  and  $\text{pEW}(t = \infty) = \text{pEW}(z = 0)$ , resulting in

$$\text{pEW}(3000 \text{ Å}) = \frac{112e^{0.938t}}{3.54 \times 10^4 + 3.16(e^{0.938t} - 1)} \text{ Å}, \quad (3)$$

which is also shown in Figure 14. This equation yields a transition time,  $t_{tr} = 9.9$  Gyr, where the feature is at half its current strength. This corresponds to  $z_{tr} = 0.34$ . However, considering systematic errors, we believe that the feature is consistent with having no change over time.

The analysis of the  $\sim 3000$  Å absorption is hampered by a lack of low-redshift UV spectra. Examining individual spectra, we see a range of strength from strong absorption (SN 1992A; Kirshner et al. 1993) to emission at this wavelength (SN 1990N; Jeffery et al. 1992). All low-redshift objects (including those without light-curve information, which are not included in any composite spectra) show this feature in absorption in at least one spectrum. However, because this wavelength can show both absorption and emission, a composite spec-

trum from SNe Ia could produce a lack of absorption (similar to the ESSENCE spectra). Without a better understanding of this feature and its strength in the low-redshift sample, we do not have the ability to make any claims of its variation between low and high redshift.

### 5.2.2. Fe III 5129

The one substantial difference between the low- $\Delta$  ESSENCE and Lick composite spectra is the strength of the Fe II 4800 feature. The Fe II 4800 feature is a blend of many lines, with the strongest being Fe II, Si II, and Fe III. Examining Figures 5 and 9, we see that the major difference in this feature between the ESSENCE and Lick composite spectra is the reddest portion, attributed to Fe III  $\lambda$ 5129. This feature is weaker in both the higher-redshift and the low- $\Delta$  binned ESSENCE spectra. The average redshift for the low- $\Delta$  composite spectrum ( $z = 0.51$ ) is significantly larger than the total composite spectrum ( $z = 0.37$ ) and the normal-luminosity composite spectrum ( $z = 0.27$ ). Similarly, as seen in Figure 15, the average  $\Delta$  decreases with redshift ( $\Delta = -0.05, 0.20, -0.14$ , and  $-0.23$  for  $0 < z < 0.2$ ,  $0.2 < z < 0.4$ ,  $0.4 < z < 0.6$ , and  $z > 0.6$ , respectively).

Note that the Lick and ESSENCE low- $\Delta$  composite spectra have the same average  $\Delta$ ,  $\langle \Delta \rangle = -0.27$ . Therefore, the differences are not the effect of comparing different average parameters. However, based on our current data set, we cannot determine if (1) on average the Fe III  $\lambda$ 5129 line is weaker in all SNe Ia with increasing redshift, or (2) the feature is weaker in low- $\Delta$  SNe Ia at high redshift and the increasing influence of low- $\Delta$  objects on the sample for increasing redshifts. Because of this ambiguity, we cannot distinguish between evolution and changing demographics. To address this issue, we would need a sufficiently large sample of  $\Delta > -0.15$  SNe Ia at high redshift and  $\Delta < -0.15$  objects over the entire redshift range. This would allow us to create  $\Delta - z$  binned composite spectra. Unfortunately, our eleven low- $\Delta$  spectra and eight  $\Delta > -0.15$ ,  $z > 0.4$  (two with  $z > 0.6$ ) spectra do not allow this binning.

Fitting the Verhulst (1845) function to the Fe II 4800 feature, assuming that  $\text{pEW}(t = 0) = \text{pEW}(z = 0.65)$  and  $\text{pEW}(t = \infty) = \text{pEW}(z = 0)$ , we find

$$\text{pEW}(\text{Fe II } 4800) = \frac{226e^{0.976t}}{4.18 \times 10^4 + 5.42(e^{0.976t} - 1)} + 86.7 \text{ \AA}. \quad (4)$$

This equation has a transition time of  $t_{tr} = 9.7$  Gyr, corresponding to  $z_{tr} = 0.36$ .

As with all equivalent width measurements, one needs to examine if the line strength is changing or if the continuum level is changing. In our case, there are two sources of continuum: the strength of the “emission” lines to either side of a feature, and the galaxy light. In order to match the  $\text{pEW}(\text{Fe II } 4800)$  values for the  $z > 0.6$  ESSENCE and Lick composite spectra, the galaxy-light component of the ESSENCE spectrum would need to be underestimated by 44%. It is possible that the “emission” features on either side of the Fe II 4800 feature are weaker in the ESSENCE spectra; however, the remarkably similar maximum-light spectra at all points in the range 4000–6000 Å (except for this feature), as seen in Figure 5, argues against this.

As we did with the  $\sim 3000$  Å feature, we fit the  $\text{pEW}$

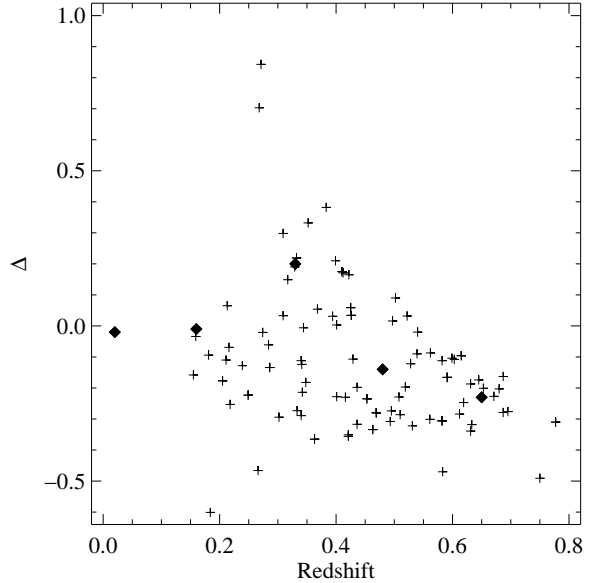


FIG. 15.—  $\Delta$  distribution of ESSENCE objects as a function of redshift. The crosses are values for individual ESSENCE objects, while the filled diamonds are the values for the redshift-binned composite spectra (including the Lick composite spectra). The lack of high- $\Delta$  objects at high redshift is the result of selection bias.

measurements from individual spectra as a function of time for both samples. The EW measurements for the ESSENCE and Lick samples (with galaxy light added to best match the ESSENCE sample) are presented in Figure 16. We only look at the data for  $t < 5$  d, which is both where the data are linear and where the line is dominated by the same absorption features. Linear fits were performed for both the Lick and ESSENCE samples with the best fits shown in Figure 16. The confidence contours associated with the linear fits are plotted in Figure 17. The two samples are different at less than the  $1\sigma$  level. We also considered the Lick sample using the PCA-reconstructed galaxy spectrum instead of the template-galaxy spectrum. As seen in Figure 7, this results in a slightly smaller  $\text{pEW}$ . Regardless of the galaxy template used, with any reasonable value of galaxy contamination the samples are still different at the  $\sim 2\sigma$  level.

The galaxy contamination is a difficult issue. Ideally, we would be able to remove the galaxy contamination in each spectrum. However, with the low S/N and small wavelength range of each individual spectrum and the uncertainty in the amount of galaxy contamination, we would need to make large assumptions about the overall continuum shape of each SN spectrum. Our method of matching the composite spectra avoids these issues by comparing high S/N spectra covering a large wavelength range. A test of the accuracy of this method is to examine the photometric fluxes of the galaxies and SNe at maximum light. From our light curves, we are able to determine the galaxy contamination in the observed  $R$  band. Then, assuming the SN spectrum is the Lick maximum-light composite spectrum, we can determine the galaxy contamination in the Fe II 4800 feature. Doing this, we find that the galaxy contamination has median and mean values of 17–19% and 22–23%, respectively, regardless of galaxy template. The  $1\sigma$  upper limit

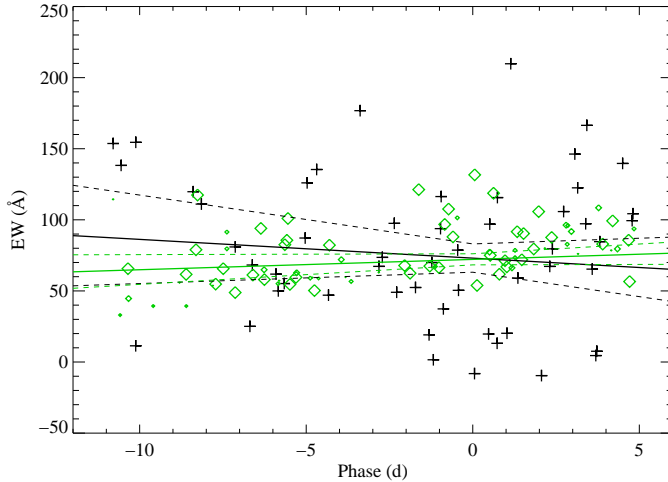


FIG. 16.— The EW measurements of Fe II 4800 for individual spectra in the ESSENCE and Lick spectra. The black crosses are for ESSENCE spectra and the green diamonds are for Lick data. The size of the points is proportional to their weight. The best-fit lines are solid black and green lines for ESSENCE and Lick, respectively. The dashed lines are the  $1\sigma$  errors in the fits. Each Lick spectrum was given a weight of  $1/N$ , where  $N$  is the number of spectra from that object used in the fit. This weights each object, rather than each spectrum, equally.

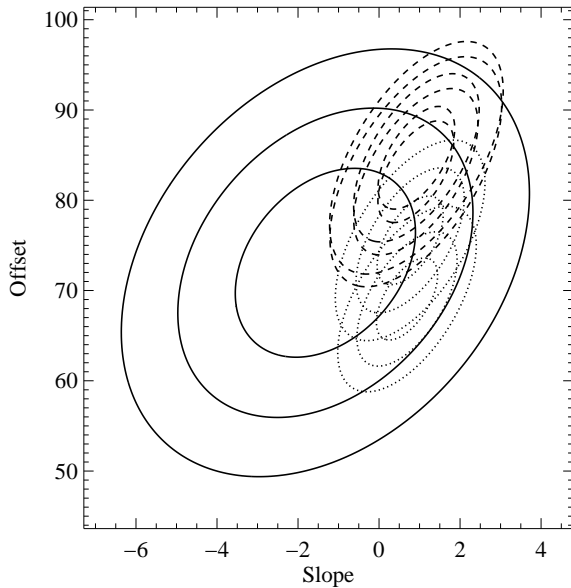


FIG. 17.—  $1\sigma$ ,  $2\sigma$ , and  $3\sigma$  confidence contours for the linear fit parameters for the Fe II 4800 feature. The large, solid contours are for the ESSENCE sample and the dashed and dotted contours are for the Lick sample. The dashed and dotted contours are from the  $1\sigma$  extremes for galaxy contamination using the Sb and Sc templates, respectively. The contours from the best-fit galaxy contamination are not plotted for clarity, but are close to averages between the plotted contours.

is 47–60% for all galaxy templates. Considering that we remove some galaxy light from our spectra while reducing our data, we regard these values as upper limits. This is consistent with what we have found from matching the low and high-redshift composite spectra.

A separate way of examining the Fe lines which avoids the majority of galaxy contamination is a ratio of the depths of the Fe II and Fe III lines. We measured the

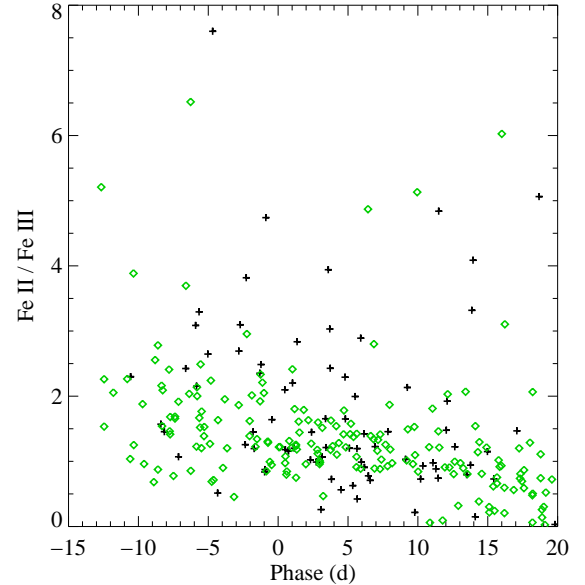


FIG. 18.— The Fe II/Fe III ratio for spectra in the ESSENCE (black crosses) and Lick (green diamonds) samples.

depths of these lines from a line segment connecting the maxima on either side of the feature, similar to the method of determining the  $\mathcal{R}(\text{Si})$  ratio first presented by Nugent et al. (1995). Since the ESSENCE spectra have low S/N, finding a true minimum for the Fe III line is difficult. We therefore measured the depth of Fe III for all spectra at the wavelength of the minimum in the Lick maximum-light composite spectrum. If this wavelength is slightly off the true minimum, causing the flux of the edge of the line to be measured, we would underestimate the true Fe III depth, leading to a larger Fe II/Fe III ratio for any given spectrum; however, since all spectra were treated in the same way, this should not significantly influence the results. The values of this ratio are presented in Figure 18, showing that this ratio evolves linearly with age, with the ESSENCE sample having a slightly larger Fe II/Fe III ratio on average. However, if we perform a two-dimensional Kolmogorov-Smirnov test, the samples are different at the 95% level, consistent with a  $\sim 2\sigma$  difference.

There are two possible physical explanations for a weaker Fe III line in high-redshift SNe Ia. The first is that high-redshift SNe Ia have lower photospheric temperatures (on average) than their low-redshift counterparts. The typical photospheric temperature of maximum-light SNe Ia is 10,000 K, which is very close to the transition between Fe II dominance and Fe III dominance (Hatano et al. 1999). A temperature change of 1000 K can dramatically change the ratio of the Fe lines. This effect has been used to explain the strong Fe III lines in SN 1991T (Filippenko et al. 1992).

An alternative explanation is that the weaker Fe III line is the result of lower metallicity. Höflich et al. (1998) shows that the physical quantity most sensitive to changing metallicity is the  $^{54}\text{Fe}$  production. As metallicity decreases,  $Y_e$ , the electron fraction, increases. This, in turn, causes less  $^{54}\text{Fe}$  production. Hatano et al. (2002) suggests that the distribution of the Fe isotopes within the SN ejecta cause Fe II lines to be generated by  $^{56}\text{Fe}$ ,



while Fe III lines come from  $^{54}\text{Fe}$ . Therefore, the weaker Fe III  $\lambda 5129$  line may be an indication of lower metallicity for high-redshift SN Ia progenitors. Sauer et al. (2008) offers a slightly different explanation: as metallicity decreases, there is less backwarming from UV photons, which decreases the temperature and significantly reduces the Fe III/Fe II ratio. In both models, lower metallicity has the same effect: weaker Fe III lines.

Finally, the red portion of the entire feature may be dominated by a species different from Fe III, such as Si II or Fe II. Although this is a possibility, it would require small blueshifts ( $v < 5000 \text{ km s}^{-1}$ ) for those lines.

### 5.2.3. Si II $\lambda 6355$

A visual inspection of the Si II  $\lambda 6355$  line shows that the placement of the continuum of the red wing of the line is causing the differences between the ESSENCE and Lick maximum-light composite spectra. Although this may be a real difference, the galaxy light is comparable to the SN component for wavelengths redward of  $6000 \text{ \AA}$ . Therefore, the comparison of the ESSENCE and Lick spectra is highly dependent on the galaxy spectrum. If we examine the feature when using the PCA-reconstructed galaxy spectrum to contaminate the Lick composite spectrum, the difference is much smaller. Considering this, and also that other lines from intermediate-mass elements (including Si II  $\lambda 4130$ ) do not show different pEWs between the Lick and ESSENCE spectra, we do not believe the Si II difference is significant. We do, however, suggest that the differences in the premaximum Si II  $\lambda 6355$  line (outlined in Section 5.3) are probably real and significant.

### 5.3. Metallicity

The two best observables for determining metallicity differences in SN Ia spectra are the velocity and depth of the Si II  $\lambda 6355$  line and the UV flux level (Höflich et al. 1998; Lentz et al. 2000). As metallicity increases, the opacity of the ejecta increases, and consequently the velocity of the Si II line becomes more blueshifted while the line strengthens. As already discussed in Section 1, the effect of changing metallicity on the UV continuum is disputed. Rather than trying to determine the correct model, we first note that all models show a change in the UV continuum with changing metallicity. In the Lentz et al. (2000) model, with increasing metallicity, there is more metal-line cooling, creating a redder SED, and at the same time, there is more line blanketing from metal lines in the blue, absorbing the flux at those wavelengths. The combination of these effects creates a UV deficit at high metallicity. Moreover, differing density structures can cause these lines to form at smaller radii, decreasing the UV flux level with increasing metallicity (Höflich et al. 1998; Domínguez et al. 2001).

As described by Lentz et al. (2000), most metallicity effects are easier to observe at early times. As seen in Section 4.5, the premaximum ESSENCE spectrum has both a stronger Si II  $\lambda 6355$  line with a larger velocity, and a UV excess, compared to the Lick premaximum composite spectrum. Unfortunately, the wavelength region where we can easily differentiate the models by UV flux is at  $\sim 2000 \text{ \AA}$ , which is blueward of our spectra. However, the general trend of the Lentz et al. (2000) models is that the UV flux level decreases with increasing

metallicity. If this is the case, then the ESSENCE objects would have lower metallicity than the Lick objects. However, using the results of Höflich et al. (1998) one would arrive at the opposite conclusion — namely, the ESSENCE objects have higher metallicity than the Lick objects. According to the Lentz et al. (2000) models, the stronger, more-blueshifted Si II  $\lambda 6355$  in the ESSENCE composite spectrum is suggestive of higher metallicities, conflicting with the UV excess.

The idea of higher metallicity for high-redshift SNe Ia is counterintuitive. However, there is a possible explanation if we consider the two-channel model for SN Ia progenitors (Mannucci et al. 2005; Scannapieco & Bildsten 2005). Examining an extreme example, suppose that at  $z = 0$  all SNe Ia come from a delayed channel and at  $z = 0.5$  all SNe Ia come from a prompt channel (an approximation of reality; Sullivan et al. 2006), which we will assume to have no delay time for simplicity. Since the light travel time from  $z = 0.5$  to  $z = 0$  is 5 Gyr, if the delay time for the delayed channel is  $> 5$  Gyr, then the low-redshift SNe Ia would come from lower-metallicity progenitors. However, the data suggest that the difference in delay times is  $\sim 2$  Gyr (Scannapieco & Bildsten 2005).

There are two major possible sources of systematic error. First, the shape of the UV continuum is, to some degree, dependent on the galaxy spectrum we fit to the ESSENCE spectrum. If we have used the incorrect galaxy type or an incorrect amount of galaxy light (both of which may vary over our wavelength range), our UV continuum could be undersubtracted, causing the UV excess. However, the UV flux of galaxies is small compared to the optical flux. Hence, if we have undersubtracted galaxy light in the UV, we would expect the effect to be even stronger in the optical, which it is not. However, if our lower-redshift premaximum spectra tended to come from SNe in early-type galaxies and our higher-redshift premaximum spectra tended to come from SNe in late-type galaxies, then the UV portion of the spectrum (which is only visible in the higher-redshift spectra) could be contaminated by relatively bluer galaxy light, for which we may not correctly account.

The other possible source of systematic error is the scarcity of premaximum low-redshift UV spectra. There are 6 spectra contributing to the UV portion of the Lick premaximum composite spectrum (1 from SN 1989B, 4 from SN 1990N, and 1 from SN 1992A). If these objects are atypical, having less UV flux than most SNe Ia at early times, the UV “excess” in the ESSENCE spectrum would simply be an artifact of comparing to these atypical objects. An argument against this is that spectra of SNe 1990N and 1992A are included in other Lick composite spectra with different phase binning (such as the maximum-light spectrum), and they do not have significantly depressed UV flux.

This result requires us to look at the other spectra in detail, searching for additional clues of a difference in metallicity. As seen in Figures 5, 9, 11, and 12, there are no other obvious UV excesses or extraordinary line velocities. As discussed in Section 5.2.2, the difference in the Fe III line may be the result of differing metallicity. Since the outer layers of the progenitor are most affected by metallicity and these layers are only seen at very early times, a noticeable change of metallicity

may not be possible for times past maximum brightness. Domínguez et al. (2001) suggests that the  $B - V$  color at maximum light decreases with increasing metallicity. They show that  $\Delta(B - V) = 0.05$  mag for metallicity increasing from  $\log(Z/Z_\odot) = -10$  to  $-1.7$ . We measure  $B - V = 0.22$  mag and  $0.24$  mag for the ESSENCE and galaxy-contaminated Lick maximum-light composite spectra, respectively, suggesting that this effect may be present in our spectra. Unfortunately, the galaxy-light contamination reduces our ability to measure accurate colors from the spectra, so we cannot determine with any certainty if this effect is real.

One place one might expect to see more pronounced evolutionary effects is in the low- $\Delta$  objects. Overluminous SNe Ia are found in star-forming galaxies (Hamuy et al. 2000; Howell 2001). Based on SN rates, Mannucci et al. (2005) and Scannapieco & Bildsten (2005) have suggested that there exist two channels for SNe Ia: short ( $\sim 1$  Gyr) and long ( $\gtrsim 3$  Gyr) delays. The SN rate from the short-delay channel is proportional to star formation. These data suggest that overluminous SNe Ia tend to come from a short-delay progenitor channel, from which the progenitor is more biased by galactic environment, and thus galactic evolution, than the long-delay channel. As star-forming galaxies increase their metallicities with time, they imprint that information in the SN Ia progenitors, creating somewhat different spectra at high and low redshift.

Comparing the UV spectra of both the ESSENCE and Lick low- $\Delta$  composite spectra, we see no UV flux differences in a subsample that should be particularly sensitive to these changes. However, the low- $\Delta$  sample is where the Fe III  $\lambda 5129$  line changes the most between low and high redshift. Although we cannot say definitively if this is the result of evolution or changing sample demographics, we see that the high- $\Delta$  Lick and ESSENCE composite spectra have weak Fe III, with the ESSENCE composite spectra weaker than the Lick spectra. If the high- $\Delta$  objects come from an old progenitor population, the ESSENCE low- $\Delta$  objects from an intermediate-age population, and the Lick low- $\Delta$  objects from a young population, the Fe III line may be the tracer of the metallicity evolution through these populations. A more appropriate subsampling, which might yield more definitive results, may be based on the host-galaxy star-formation rate (Sullivan et al. 2006; Howell et al. 2007).

#### 5.4. K-Corrections

One of the largest systematic errors associated with SN distance determinations is the uncertainty in the K-corrections. Ideally, one would have a time sequence of perfectly flux-calibrated, contamination-free spectra (either for the object or for all template objects) to synthesize light curves that perfectly match the observed bands in the frame of the object. Since getting multiple-epoch spectra of numerous low-redshift objects or obtaining multiple-epoch spectra of a single high-redshift SN is very time consuming, we implement K-corrections to match photometric observations of high-redshift SNe to those of low-redshift SNe. If there is a small difference between the SED of the high-redshift SN and its low-redshift counterpart near the edge of the filter transmission function, errors in the magnitudes (and thus overall distance) are introduced.

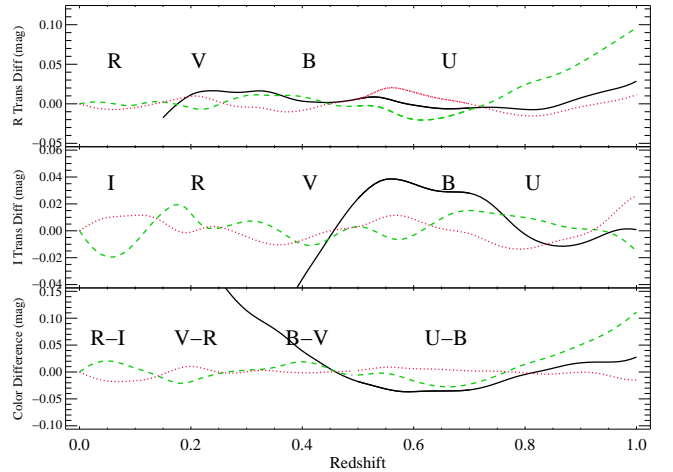


FIG. 19.— The difference between maximum-light synthetic rest-frame  $UBVR$  and K-corrected synthetic observed-frame  $R$ -band and  $I$ -band photometry. The black curve is the difference between the ESSENCE composite spectrum and the Lick template. The green (dashed) and red (dotted) curves are the difference between the Lick composite spectrum and the Nugent and SNLS templates, respectively.

One method of determining the K-corrections for a particular object consists of using a template low-redshift spectrum, warping it to the observed colors of the high-redshift SN, and then determining the comparable rest-frame magnitudes (Kim et al. 1996; Nugent et al. 2002). This method is particularly sensitive to differences between SEDs.

In order to determine the impact of using one particular spectral template for K-corrections, we warped the Nugent and SNLS templates and the Lick and ESSENCE composite spectra to have the same rest-frame colors, redshifted the spectra, and extracted synthetic photometry. The warping is dependent on where the anchor points are placed, but this is not critical for our applications. We extracted  $R$ -band and  $I$ -band magnitudes for all three spectra over a redshift range of  $0 < z < 1$ . Because of its bluer rest-frame wavelength range, the ESSENCE spectrum cannot be used for the lowest redshifts. Furthermore, as seen in Figure 5, the large uncertainty in the ESSENCE spectrum at red wavelengths makes the  $I$ -band magnitudes for  $z < 0.5$  unreliable.

As seen in Figure 19, all four spectra are generally consistent to  $\pm 0.02$  mag. The main deviation between the Lick composite and Nugent template is at  $z > 0.8$ , where the near-UV is redshifted into the  $R$  band. The differences between the spectra in the UV (as seen in Figure 4) create this large difference. The SNLS template is more consistent with both the Lick and ESSENCE composite spectra.

This analysis shows that the systematic error associated with K-corrections is small but non-negligible, with  $\sigma_K \approx 0.01$ – $0.02$  mag for  $z < 1$ , consistent with that found by Hsiao et al. (2007), but larger than that assumed by Wood-Vasey et al. (2007). We also note that the Nugent template has large differences compared to both the Lick and ESSENCE composite spectra; it should not be used for SNe with  $z > 0.8$ .

#### 5.5. Constraining Evolution

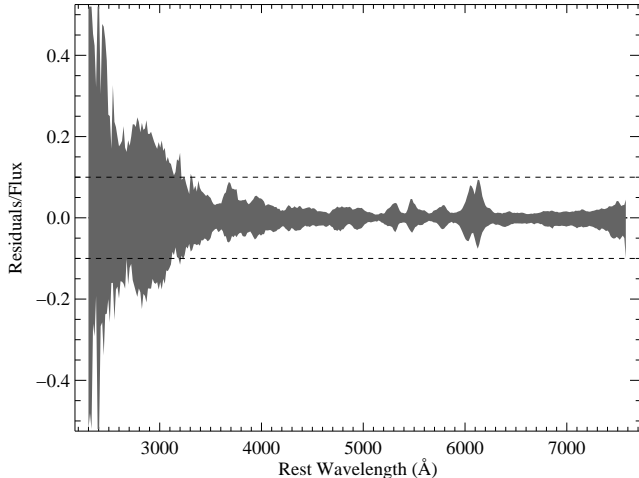


FIG. 20.— The percent variation in the Lick maximum-light composite spectrum. The dashed lines are the  $\pm 10\%$  variation. The variation is larger at shorter wavelengths.

Ultimately, studies of SN evolution are aimed at determining how the luminosity of the average SN Ia changes with redshift. The change in luminosity will directly affect our measurements of SN distances, and thus measurements of cosmological parameters. Currently, the systematic error associated with SN evolution is estimated to be  $< 0.02$  mag, corresponding to an error of 0.02 in measuring  $w$ , the equation-of-state parameter for dark energy. With our composite spectra, we have the first way to quantify this error.

In Figure 20, we show the percent variation (the ratio of the  $1\sigma$  error residuals to the SN flux) for the Lick maximum-light composite spectrum. For most optical wavelengths, these values are dominated by the intrinsic variation of the SN spectra. In the UV, however, the noise in the composite spectrum from the small number of spectra dominates over the variance amongst objects. It is noteworthy that for wavelengths in the range of 3200–4000 Å, the variation is larger than for longer wavelengths and increasing with smaller wavelengths. This has been seen photometrically as a relatively large variation in the  $U$ -band light curves of nearby objects (Jha et al. 2006). We therefore expect this intrinsic variation to continue to increase into the UV.

We see that the intrinsic variation of SN spectra is at  $\sim 3\%$  for most of the optical range. Binning over larger wavelengths, the variation in individual features will average out, causing the extremes of this variation to decrease slightly. In Figure 21, we show the difference in observed  $R$ -band magnitudes of the  $1\sigma$  variance spectra. This measurement is an indication of the variation of the spectra at maximum light and not the peak luminosity, since we have normalized our spectra to have the same flux at a particular wavelength. For  $z > 0.4$ , we see that the difference increases with redshift as the rest-frame UV is redshifted into the observed-frame  $R$  band. This is probably an overestimate of the maximum difference, since most spectra will vary within the  $1\sigma$  range rather than being at either the high or low end.

We also present the percent variation for the ESSENCE maximum-light composite spectrum in Figure 22. For most of the rest-frame optical, the variation

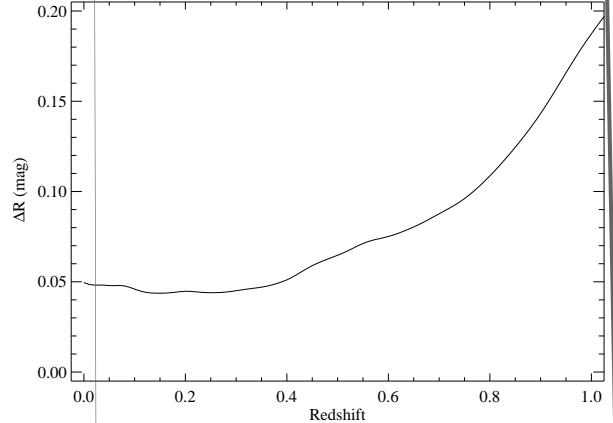


FIG. 21.— The difference in measured  $R$ -band magnitudes for the upper and lower  $1\sigma$  variance Lick maximum-light composite spectrum with redshift. This difference indicates an upper limit on the  $R$ -band difference after already normalizing the spectra as described in Section 3.

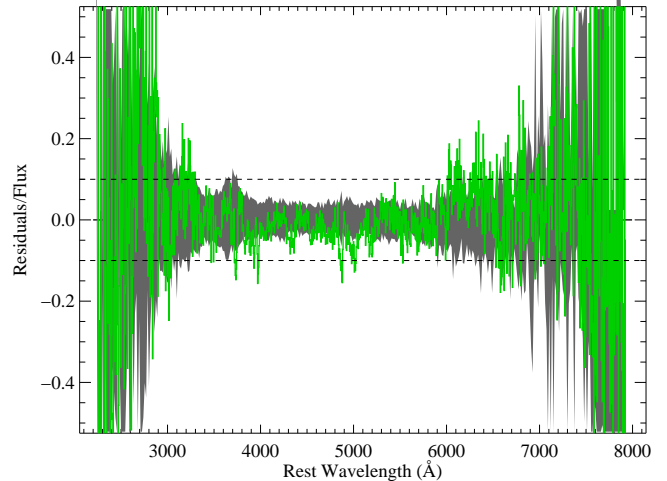


FIG. 22.— The percent variation in the ESSENCE maximum-light composite spectrum in grey. The green line is the percent variation of the residuals of the Lick maximum-light composite spectrum (as seen in Figure 5). The dashed lines are the  $\pm 10\%$  variation.

is  $\sim 5\%$ . It is possible that the high-redshift sample has a larger intrinsic variation than the Lick sample, but it is more likely that the variation is dominated by the different amounts of galaxy contamination and noise in the spectra. Figure 22 also shows that the difference between the Lick and ESSENCE maximum-light composite spectra differs by  $\lesssim 10\%$  over most of the rest-frame optical. We can therefore constrain evolution between our two samples to  $\sim 10\%$  across the spectrum.

## 6. CONCLUSIONS

By combining many low-S/N, high-redshift SN Ia spectra, we are able to construct the first series of composite SN Ia spectra based on the parameters of redshift, phase,  $\Delta$ , and  $A_V$ . In addition, we constructed similar composite spectra from a high-quality sample of low-redshift SN Ia spectra obtained over the last two decades. Comparison of the composite spectra has shown that once we account for galaxy-light contamination, the two samples are remarkably similar. There are several minor devia-

tions between low and high-redshift samples. These deviations fall into three categories: related to metallicity, related to  $^{56}\text{Ni}$  production, and unknown.

The UV excess in the ESSENCE premaximum spectrum is indicative of a different metallicity for the low and high-redshift SNe. Depending on the model, a UV excess is the result of higher or lower metallicity (Höflich et al. 1998; Lentz et al. 2000). The stronger, more blueshifted Si II  $\lambda 6355$  line in the ESSENCE premaximum spectrum indicates a higher metallicity (Lentz et al. 2000).

The most significant difference between our samples is the varying strength of the Fe III  $\lambda 5129$  line. The evolution of the Fe III line may indicate that high-redshift SNe Ia have lower temperatures than low-redshift SNe Ia. This, in turn, suggests that SNe Ia should be less luminous at high redshift. The weak Fe III line may indicate lower  $^{54}\text{Fe}$  production, which could be the result of lower metallicity. Alternatively, lower metallicity may cause less backwarming from UV photons, decreasing the temperature and the Fe III/Fe II ratio. It is unclear if this difference is from evolution in all SNe Ia, evolution just in the low- $\Delta$  SNe Ia, changing demographics, or a selection effect. Low- $\Delta$  SNe Ia tend to come from the short-delay progenitor channel. Because of the short delay, the progenitors of these SNe are more biased by galactic environment, and thus galactic evolution, than the progenitors of long-delay channel SNe Ia. It is therefore not surprising that the difference in the Fe III line is more obvious in the low- $\Delta$  objects.

It is possible that the different strengths of the  $\sim 3000$  Å Fe II feature between low and high redshift is an artifact of the construction of the composite spectra. An analysis of the individual spectra of both samples indicates that the samples are not significantly different; however, the small number of UV objects hampers this study.

It is difficult to definitively detect metallicity differences between the Lick and ESSENCE samples. First, we have observed three differences between the samples which harbingers a difference in metallicity: a UV excess, a stronger and more blueshifted Si II  $\lambda 6355$  line, and a weaker Fe III  $\lambda 5129$  line. The UV excess is an ambiguous indicator since the models disagree if it indicates lower or higher metallicity. The Si II line in the premaximum spectrum suggests higher metallicity, and the Fe III line suggests lower metallicity.

We have also shown that the previously published low-redshift template spectra have multiple drawbacks when comparing to high-redshift composite spectra. We therefore caution against using these templates for studies of SN Ia evolution. Furthermore, deriving K-corrections from any low-redshift template is difficult; however, the systematic errors are likely to be relatively small.

We see that the intrinsic variation of low-redshift SN spectra is  $\sim 3\%$  in the optical. The spectra vary more in the near-UV and UV as suggested by photometry (Jha et al. 2006). We are able to put the first constraints of SN Ia evolution to  $\lesssim 10\%$ .

The results of this study are very suggestive, but require further investigation. In order to improve our understanding of SN Ia evolution, we propose three future studies related to this work. First, the theoretical models of the effects of metallicity on SN Ia spectra should be expanded. With the current ambiguity amongst models, we cannot determine the direction of the trend in

metallicity. Second, we should gather many more high-redshift spectra to disentangle the redshift- $\Delta$  ambiguity. Finally, further UV observations of nearby SNe Ia are desperately needed. The only current instrument available for the task is the *Swift* UVOT. However, previous attempts at obtaining SN Ia UV spectra have been disappointing (Brown et al. 2005). We suggest an intense campaign spending several hours per spectrum (similar to *IUE*) with the UVOT. In the near future, we may once again have the ability to obtain high-quality UV spectra with *HST* using *STIS* or *COS*. If the upcoming *HST* servicing mission is successful, we strongly suggest a massive campaign to observe local SNe Ia in the UV. Since *JWST* does not have the capabilities to observe the UV, this may be our last opportunity for many years.

Based in part on observations obtained at the Cerro Tololo Inter-American Observatory, which is operated by the Association of Universities for Research in Astronomy, Inc. (AURA) under cooperative agreement with the National Science Foundation (NSF); the European Southern Observatory, Chile (ESO Programmes 170.A-0519 and 176.A-0319); the Gemini Observatory, which is operated by the Association of Universities for Research in Astronomy, Inc., under a cooperative agreement with the NSF on behalf of the Gemini partnership: the NSF (United States), the Particle Physics and Astronomy Research Council (United Kingdom), the National Research Council (Canada), CONICYT (Chile), the Australian Research Council (Australia), CNPq (Brazil), and CONICET (Argentina) (Programs GN-2002B-Q-14, GS-2003B-Q-11, GN-2003B-Q-14, GS-2004B-Q-4, GN-2004B-Q-6, GS-2005B-Q-31, GN-2005B-Q-35); the Magellan Telescopes at Las Campanas Observatory; the MMT Observatory, a joint facility of the Smithsonian Institution and the University of Arizona; and the F. L. Whipple Observatory, which is operated by the Smithsonian Astrophysical Observatory. Some of the data presented herein were obtained at the W. M. Keck Observatory, which is operated as a scientific partnership among the California Institute of Technology, the University of California, and the National Aeronautics and Space Administration; the Observatory was made possible by the generous financial support of the W. M. Keck Foundation. Most of the low-redshift SN Ia spectra used here were obtained by A.V.F.’s group over the course of two decades with the 3-m Shane reflector at Lick Observatory. We thank the Lick staff for their dedicated help, as well as many graduate students for assistance with the observations and reductions.

The ESSENCE survey team is very grateful to the scientific and technical staff at the observatories we have been privileged to use.

*Facilities:* Blanco (MOSAIC II), CTIO:0.9m (CFCCD), Gemini:South (GMOS), Gemini:North (GMOS), Keck:I (LRIS), Keck:II (DEIMOS, ESI), Lick:3m Shane (UV Schmidt, Kast), VLT (FORIS1), Magellan:Baade (IMACS), Magellan:Clay (LDSS2).

The survey is supported by the US National Science Foundation through grants AST-0443378 and AST-0507475. The Dark Cosmology Centre is funded by the Danish National Research Foundation. S.J. thanks the Stanford Linear Accelerator Center for support via a

Panofsky Fellowship. A.R. thanks the NOAO Goldberg fellowship program for its support. P.M.G. is supported in part by NASA Long-Term Astrophysics Grant NAG5-9364 and NASA/HST Grant GO-09860. R.P.K. enjoys support from AST06-06772 and PHY99-07949 to the Kavli Institute for Theoretical Physics. A.C. acknowledges the support of CONICYT, Chile, under grants FONDECYT 1051061 and FONDAF Center for Astro-

physics 15010003. A.V.F.'s supernova group at U.C. Berkeley has been supported by many NSF grants over the past two decades, most recently AST-0307894 and AST-0607485.

Our project was made possible by the survey program administered by NOAO, and builds upon the data-reduction pipeline developed by the SuperMacho collaboration.

## REFERENCES

- Altavilla, G., Ruiz-Lapuente, P., Balastegui, A., Mendez, J., Irwin, M., Espana-Bonet, C., Schamaneche, K., Balland, C., Ellis, R. S., Fabbro, S., Folatelli, G., Goobar, A., Hillebrandt, W., McMahon, R. M., Mouchet, M., Mourao, A., Nobili, S., Pain, R., Stanishev, V., & Walton, N. A. 2006, *ArXiv Astrophysics e-prints*
- Astier, P., Guy, J., Regnault, N., Pain, R., Aubourg, E., Balam, D., Basa, S., Carlberg, R. G., Fabbro, S., Fouchez, D., Hook, I. M., Howell, D. A., Lafoux, H., Neill, J. D., Palanque-Delabrouille, N., Perrett, K., Pritchet, C. J., Rich, J., Sullivan, M., Taillet, R., Aldering, G., Antilogus, P., Arsenijevic, V., Balland, C., Baumont, S., Bronder, J., Courtois, H., Ellis, R. S., Filiol, M., Gonçalves, A. C., Goobar, A., Guide, D., Hardin, D., Lusset, V., Lidman, C., McMahon, R., Mouchet, M., Mourao, A., Perlmutter, S., Ripoche, P., Tao, C., & Walton, N. 2006, *A&A*, 447, 31
- Balland, C., Mouchet, M., Amanullah, R., Astier, P., Fabbro, S., Folatelli, G., Garavini, G., Goobar, A., Hardin, D., Irwin, M. J., McMahon, R. G., Mourao, A.-M., Nobili, S., Pain, R., Pascoal, R., Raux, J., Sainton, G., Schahmaneche, K., & Walton, N. A. 2007, *A&A*, 464, 827
- Blondin, S., Dessart, L., Leibundgut, B., Branch, D., Höflich, P., Tonry, J. L., Matheson, T., Foley, R. J., Chornock, R., Filippenko, A. V., Sollerman, J., Spyromilio, J., Kirshner, R. P., Wood-Vasey, W. M., Clocchiatti, A., Aguilera, C., Barris, B., Becker, A. C., Challis, P., Covarrubias, R., Davis, T. M., Garnavich, P., Hicken, M., Jha, S., Krisciunas, K., Li, W., Miceli, A., Miknaitis, G., Pignata, G., Prieto, J. L., Rest, A., Riess, A. G., Salvo, M. E., Schmidt, B. P., Smith, R. C., Stubbs, C. W., & Suntzeff, N. B. 2006, *AJ*, 131, 1648
- Blondin, S., Walsh, J. R., Leibundgut, B., & Sainton, G. 2005, *A&A*, 431, 757
- Branch, D., & Venkatakrishna, K. L. 1986, *ApJ*, 306, L21
- Bronder, T. J., Hook, I. M., Astier, P., Balam, D., Balland, C., Basa, S., Carlberg, R. G., Conley, A., Fouchez, D., Guy, J., Howell, D. A., Neill, J. D., Pain, R., Perrett, K., Pritchet, C. J., Regnault, N., Sullivan, M., Baumont, S., Fabbro, S., Filiol, M., Perlmutter, S., & Ripoche, P. 2007, *ArXiv e-prints*, 709
- Brown, P. J., Holland, S. T., James, C., Milne, P., Roming, P. W. A., Mason, K. O., Page, K. L., Beardmore, A. P., Burrows, D., Morgan, A., Gronwall, C., Blustin, A. J., Boyd, P., Still, M., Breeveld, A., de Pasquale, M., Hunsberger, S., Ivanushkina, M., Landsman, W., McGowan, K., Poole, T., Rosen, S., Schady, P., & Gehrels, N. 2005, *ApJ*, 635, 1192
- Buta, R. J., Corwin, Jr., H. G., & Opal, C. B. 1985, *PASP*, 97, 229
- Cardelli, J. A., Clayton, G. C., & Mathis, J. S. 1989, *ApJ*, 345, 245
- Ciatti, F., Barbon, R., Cappellaro, E., & Rosino, L. 1988, *A&A*, 202, 15
- Cimatti, A., Daddi, E., Renzini, A., Cassata, P., Vanzella, E., Pozzetti, L., Cristiani, S., Fontana, A., Rodighiero, G., Mignoli, M., & Zamorani, G. 2004, *Nature*, 430, 184
- Coil, A. L., Matheson, T., Filippenko, A. V., Leonard, D. C., Tonry, J., Riess, A. G., Challis, P., Clocchiatti, A., Garnavich, P. M., Hogan, C. J., Jha, S., Kirshner, R. P., Leibundgut, B., Phillips, M. M., Schmidt, B. P., Schommer, R. A., Smith, R. C., Soderberg, A. M., Spyromilio, J., Stubbs, C., Suntzeff, N. B., & Woudt, P. 2000, *ApJ*, 544, L111
- Conley, A., Carlberg, R. G., Guy, J., Howell, D. A., Jha, S., Riess, A. G., & Sullivan, M. 2007, *ApJ*, 664, L13
- Domínguez, I., Höflich, P., & Straniero, O. 2001, *ApJ*, 557, 279
- Efron, B. 1982, *The Jackknife, the Bootstrap and other resampling plans* (CBMS-NSF Regional Conference Series in Applied Mathematics, Philadelphia: Society for Industrial and Applied Mathematics (SIAM), 1982)
- Filippenko, A. V. 2005, in *Astrophysics and Space Science Library*, Vol. 332, *White dwarfs: cosmological and galactic probes*, ed. E. M. Sion, S. Vennes, & H. L. Shipman, 97–133
- Filippenko, A. V., Richmond, M. W., Matheson, T., Shields, J. C., Burbidge, E. M., Cohen, R. D., Dickinson, M., Malkan, M. A., Nelson, B., Pietz, J., Schlegel, D., Schmeer, P., Spinrad, H., Steidel, C. C., Tran, H. D., & Wren, W. 1992, *ApJ*, 384, L15
- Foley, R. J. et al. 2008a, in prep.
- . 2008b, in prep.
- Foley, R. J., Filippenko, A. V., Leonard, D. C., Riess, A. G., Nugent, P., & Perlmutter, S. 2005, *ApJ*, 626, L11
- Gallagher, J. S., Garnavich, P. M., Berlind, P., Challis, P., Jha, S., & Kirshner, R. P. 2005, *ApJ*, 634, 210
- Ganeshalingam, M. et al. 2008, in prep.
- Garavini, G., Folatelli, G., Nobili, S., Aldering, G., Amanullah, R., Antilogus, P., Astier, P., Blanc, G., Bronder, J., Burns, M. S., Conley, A., Deustua, S. E., Doi, M., Fabbro, S., Fadeyev, V., Gibbons, R., Goldhaber, G., Goobar, A., Groom, D. E., Hook, I., Howell, D. A., Kashikawa, N., Kim, A. G., Kowalski, M., Kuznetsova, N., Lee, B. C., Lidman, C., Mendez, J., Morokuma, T., Motohara, K., Nugent, P. E., Pain, R., Perlmutter, S., Quimby, R., Raux, J., Regnault, N., Ruiz-Lapuente, P., Sainton, G., Schahmaneche, K., Smith, E., Spadafora, A. L., Stanishev, V., Thomas, R. C., Walton, N. A., Wang, L., Wood-Vasey, W. M., & Supernova Cosmology Project, N. Y. T. 2007, *ArXiv Astrophysics e-prints*
- Goldhaber, G., Groom, D. E., Kim, A., Aldering, G., Astier, P., Conley, A., Deustua, S. E., Ellis, R., Fabbro, S., Fruchter, A. S., Goobar, A., Hook, I., Irwin, M., Kim, M., Knop, R. A., Lidman, C., McMahon, R., Nugent, P. E., Pain, R., Panagia, N., Pennypacker, C. R., Perlmutter, S., Ruiz-Lapuente, P., Schaefer, B., Walton, N. A., & York, T. 2001, *ApJ*, 558, 359
- Hamuy, M., Phillips, M. M., Suntzeff, N. B., Schommer, R. A., Maza, J., Antezan, A. R., Wischnjewsky, M., Valladares, G., Muena, C., Gonzales, L. E., Aviles, R., Wells, L. A., Smith, R. C., Navarrete, M., Covarrubias, R., Williger, G. M., Walker, A. R., Layden, A. C., Elias, J. H., Baldwin, J. A., Hernandez, M., Tirado, H., Ugarte, P., Elston, R., Saavedra, N., Barrientos, F., Costa, E., Lira, P., Ruiz, M. T., Anguita, C., Gomez, X., Ortiz, P., della Valle, M., Danziger, J., Storm, J., Kim, Y.-C., Bailyn, C., Rubenstein, E. P., Tucker, D., Cersosimo, S., Mendez, R. A., Siciliano, L., Sherry, W., Chaboyer, B., Koopmann, R. A., Geisler, D., Sarajedini, A., Dey, A., Tyson, N., Rich, R. M., Gal, R., Lamontagne, R., Caldwell, N., Guhathakurta, P., Phillips, A. C., Szkody, P., Prosser, C., Ho, L. C., McMahon, R., Baggeley, G., Cheng, K.-P., Havlen, R., Wakamatsu, K., Janes, K., Malkan, M., Baganoff, F., Seitzer, P., Shara, M., Sturch, C., Hesser, J., Hartig, A. N. P., Hughes, J., Welch, D., Williams, T. B., Ferguson, H., Francis, P. J., French, L., Bolte, M., Roth, J., Odewahn, S., Howell, S., & Krzeminski, W. 1996, *AJ*, 112, 2408
- Hamuy, M., Trager, S. C., Pinto, P. A., Phillips, M. M., Schommer, R. A., Ivanov, V., & Suntzeff, N. B. 2000, *AJ*, 120, 1479
- Hatano, K., Branch, D., Fisher, A., Millard, J., & Baron, E. 1999, *ApJS*, 121, 233
- Hatano, K., Branch, D., Qiu, Y. L., Baron, E., Thielemann, F.-K., & Fisher, A. 2002, *New Astronomy*, 7, 441
- Hauschildt, P. H., Baron, E., Starrfield, S., & Allard, F. 1996, *ApJ*, 462, 386
- Höflich, P., Wheeler, J. C., & Thielemann, F.-K. 1998, *ApJ*, 495, 617
- Hook, I. M., Howell, D. A., Aldering, G., Amanullah, R., Burns, M. S., Conley, A., Deustua, S. E., Ellis, R., Fabbro, S., Fadeyev, V., Folatelli, G., Garavini, G., Gibbons, R., Goldhaber, G., Goobar, A., Groom, D. E., Kim, A. G., Knop, R. A., Kowalski, M., Lidman, C., Nobili, S., Nugent, P. E., Pain, R., Pennypacker, C. R., Perlmutter, S., Ruiz-Lapuente, P., Sainton, G., Schaefer, B. E., Smith, E., Spadafora, A. L., Stanishev, V., Thomas, R. C., Walton, N. A., Wang, L., & Wood-Vasey, W. M. 2005, *AJ*, 130, 2788



- Howell, D. A. 2001, *ApJ*, 554, L193
- Howell, D. A., Sullivan, M., Conley, A., & Carlberg, R. 2007, *ArXiv Astrophysics e-prints*
- Howell, D. A., Sullivan, M., Perrett, K., Bronder, T. J., Hook, I. M., Astier, P., Aubourg, E., Balam, D., Basa, S., Carlberg, R. G., Fabbro, S., Fouchez, D., Guy, J., Lafoux, H., Neill, J. D., Pain, R., Palanque-Delabrouille, N., Pritchett, C. J., Regnault, N., Rich, J., Taillet, R., Knop, R., McMahon, R. G., Perlmutter, S., & Walton, N. A. 2005, *ApJ*, 634, 1190
- Hsiao, E. Y., Conley, A., Howell, D. A., Sullivan, M., Pritchett, C. J., Carlberg, R. G., Nugent, P. E., & Phillips, M. M. 2007, *ArXiv Astrophysics e-prints*
- James, J. B., Davis, T. M., Schmidt, B. P., & Kim, A. G. 2006, *MNRAS*, 370, 933
- Jeffery, D. J., Leibundgut, B., Kirshner, R. P., Benetti, S., Branch, D., & Sonneborn, G. 1992, *ApJ*, 397, 304
- Jha, S., Kirshner, R. P., Challis, P., Garnavich, P. M., Matheson, T., Soderberg, A. M., Graves, G. J. M., Hicken, M., Alves, J. F., Arce, H. G., Balog, Z., Barmby, P., Barton, E. J., Berlind, P., Bragg, A. E., Briceño, C., Brown, W. R., Buckley, J. H., Caldwell, N., Calkins, M. L., Carter, B. J., Concannon, K. D., Donnelly, R. H., Eriksen, K. A., Fabricant, D. G., Falco, E. E., Fiore, F., Garcia, M. R., Gómez, M., Grogin, N. A., Groner, T., Groot, P. J., Haisch, Jr., K. E., Hartmann, L., Hergenrother, C. W., Holman, M. J., Huchra, J. P., Jayawardhana, R., Jerius, D., Kannappan, S. J., Kim, D.-W., Kleyna, J. T., Kochanek, C. S., Koranyi, D. M., Krockenberger, M., Lada, C. J., Luhman, K. L., Luu, J. X., Macri, L. M., Mader, J. A., Mahdavi, A., Marengo, M., Marsden, B. G., McLeod, B. A., McNamara, B. R., Megeath, S. T., Moraru, D., Mossman, A. E., Muench, A. A., Muñoz, J. A., Muzerolle, J., Naranjo, O., Nelson-Patel, K., Pahre, M. A., Patten, B. M., Peters, J., Peters, W., Raymond, J. C., Rines, K., Schild, R. E., Sobczak, G. J., Spahr, T. B., Stauffer, J. R., Stefanik, R. P., Szentgyorgyi, A. H., Tollestrup, E. V., Väisänen, P., Vikhlinin, A., Wang, Z., Willner, S. P., Wolk, S. J., Zajac, J. M., Zhao, P., & Stanek, K. Z. 2006, *AJ*, 131, 527
- Jha, S., Riess, A. G., & Kirshner, R. P. 2007, *ApJ*, 659, 122
- Kim, A., Goobar, A., & Perlmutter, S. 1996, *PASP*, 108, 190
- Kirshner, R. P., Jeffery, D. J., Leibundgut, B., Challis, P. M., Sonneborn, G., Phillips, M. M., Suntzeff, N. B., Smith, R. C., Winkler, P. F., Winge, C., Hamuy, M., Hunter, D. A., Roth, K. C., Blades, J. C., Branch, D., Chevalier, R. A., Fransson, C., Panagia, N., Wagoner, R. V., Wheeler, J. C., & Harkness, R. P. 1993, *ApJ*, 415, 589
- Kriszunas, K., Garnavich, P. M., Challis, P., Prieto, J. L., Riess, A. G., Barris, B., Aguilera, C., Becker, A. C., Blondin, S., Chornock, R., Clocchiatti, A., Covarrubias, R., Filippenko, A. V., Foley, R. J., Hicken, M., Jha, S., Kirshner, R. P., Leibundgut, B., Li, W., Matheson, T., Miceli, A., Miknaitis, G., Rest, A., Salvo, M. E., Schmidt, B. P., Smith, R. C., Sollerman, J., Spyromilio, J., Stubbs, C. W., Suntzeff, N. B., Tonry, J. L., & Wood-Vasey, W. M. 2005, *AJ*, 130, 2453
- Leibundgut, B. 2001, *ARA&A*, 39, 67
- Lentz, E. J., Baron, E., Branch, D., Hauschildt, P. H., & Nugent, P. E. 2000, *ApJ*, 530, 966
- Mannucci, F., Della Valle, M., Panagia, N., Cappellaro, E., Cresci, G., Maiolino, R., Petrosian, A., & Turatto, M. 2005, *A&A*, 433, 807
- Matheson, T., Blondin, S., Foley, R. J., Chornock, R., Filippenko, A. V., Leibundgut, B., Smith, R. C., Sollerman, J., Spyromilio, J., Kirshner, R. P., Clocchiatti, A., Aguilera, C., Barris, B., Becker, A. C., Challis, P., Covarrubias, R., Garnavich, P., Hicken, M., Jha, S., Kriszunas, K., Li, W., Miceli, A., Miknaitis, G., Prieto, J. L., Rest, A., Riess, A. G., Salvo, M. E., Schmidt, B. P., Stubbs, C. W., Suntzeff, N. B., & Tonry, J. L. 2005, *AJ*, 129, 2352
- Matheson, T. et al. 2007, in prep.
- Matheson, T., Filippenko, A. V., Ho, L. C., Barth, A. J., & Leonard, D. C. 2000, *AJ*, 120, 1499
- Matheson, T., Filippenko, A. V., Li, W., Leonard, D. C., & Shields, J. C. 2001, *AJ*, 121, 1648
- Miknaitis, G., Pignata, G., Rest, A., Wood-Vasey, W. M., Blondin, S., Challis, P., Smith, R. C., Stubbs, C. W., Suntzeff, N. B., Foley, R. J., Matheson, T., Tonry, J. L., Aguilera, C., Blackman, J. W., Becker, A. C., Clocchiatti, A., Covarrubias, R., Davis, T. M., Filippenko, A. V., Garg, A., Garnavich, P. M., Hicken, M., Jha, S., Kriszunas, K., Kirshner, R. P., Leibundgut, B., Li, W., Miceli, A., Narayan, G., Prieto, J. L., Riess, A. G., Salvo, M. E., Schmidt, B. P., Sollerman, J., Spyromilio, J., & Zenteno, A. 2007, *ApJ*, 666, 674
- Miller, J. S., & Stone, R. P. S. 1993, *Lick Obs. Tech. Rep.* 66 (Santa Cruz: Lick Obs.)
- Nomoto, K., Thielemann, F.-K., & Yokoi, K. 1984, *ApJ*, 286, 644
- Nugent, P., Kim, A., & Perlmutter, S. 2002, *PASP*, 114, 803
- Nugent, P., Phillips, M., Baron, E., Branch, D., & Hauschildt, P. 1995, *ApJ*, 455, L147+
- Panagia, N. 2007, *ArXiv e-prints*, 704
- Patat, F., Benetti, S., Cappellaro, E., Danziger, I. J., della Valle, M., Mazzali, P. A., & Turatto, M. 1996, *MNRAS*, 278, 111
- Perlmutter, S., Aldering, G., Goldhaber, G., Knop, R. A., Nugent, P., Castro, P. G., Deustua, S., Fabbro, S., Goobar, A., Groom, D. E., Hook, I. M., Kim, A. G., Kim, M. Y., Lee, J. C., Nunes, N. J., Pain, R., Pennypacker, C. R., Quimby, R., Lidman, C., Ellis, R. S., Irwin, M., McMahon, R. G., Ruiz-Lapuente, P., Walton, N., Schaefer, B., Boyle, B. J., Filippenko, A. V., Matheson, T., Fruchter, A. S., Panagia, N., Newberg, H. J. M., & Couch, W. J. 1999, *ApJ*, 517, 565
- Phillips, M. M. 1993, *ApJ*, 413, L105
- Podsiadlowski, P., Mazzali, P. A., Lesaffre, P., Wolf, C., & Forster, F. 2006, *ArXiv Astrophysics e-prints*
- Richmond, M. W., Treffers, R. R., Filippenko, A. V., Van Dyk, S. D., Paik, Y., Peng, C., Marschall, L. A., Laaksonen, B. D., Macintosh, B., & McLean, I. S. 1995, *AJ*, 109, 2121
- Riess, A. G., Filippenko, A. V., Challis, P., Clocchiatti, A., Diercks, A., Garnavich, P. M., Gilliland, R. L., Hogan, C. J., Jha, S., Kirshner, R. P., Leibundgut, B., Phillips, M. M., Reiss, D., Schmidt, B. P., Schommer, R. A., Smith, R. C., Spyromilio, J., Stubbs, C., Suntzeff, N. B., & Tonry, J. 1998, *AJ*, 116, 1009
- Riess, A. G., Filippenko, A. V., Li, W., & Schmidt, B. P. 1999a, *AJ*, 118, 2668
- Riess, A. G., Kirshner, R. P., Schmidt, B. P., Jha, S., Challis, P., Garnavich, P. M., Esin, A. A., Carpenter, C., Grashius, R., Schild, R. E., Berlind, P. L., Huchra, J. P., Prosser, C. F., Falco, E. E., Benson, P. J., Briceño, C., Brown, W. R., Caldwell, N., dell'Antonio, I. P., Filippenko, A. V., Goodman, A. A., Grogin, N. A., Groner, T., Hughes, J. P., Green, P. J., Jansen, R. A., Kleyna, J. T., Luu, J. X., Macri, L. M., McLeod, B. A., McLeod, K. K., McNamara, B. R., McLean, B., Milone, A. A. E., Mohr, J. J., Moraru, D., Peng, C., Peters, J., Prestwich, A. H., Stanek, K. Z., Szentgyorgyi, A., & Zhao, P. 1999b, *AJ*, 117, 707
- Riess, A. G., Strolger, L.-G., Casertano, S., Ferguson, H. C., Mobasher, B., Gold, B., Challis, P. J., Filippenko, A. V., Jha, S., Li, W., Tonry, J., Foley, R., Kirshner, R. P., Dickinson, M., MacDonald, E., Eisenstein, D., Livio, M., Younger, J., Xu, C., Dahlén, T., & Stern, D. 2007, *ApJ*, 659, 98
- Röpke, F. K., & Hillebrandt, W. 2004, *A&A*, 420, L1
- Sauer, D. N. et al. 2008, in prep.
- Scannapieco, E. & Bildsten, L. 2005, *ApJ*, 629, L85
- Sullivan, M., Le Borgne, D., Pritchett, C. J., Hodsman, A., Neill, J. D., Howell, D. A., Carlberg, R. G., Astier, P., Aubourg, E., Balam, D., Basa, S., Conley, A., Fabbro, S., Fouchez, D., Guy, J., Hook, I., Pain, R., Palanque-Delabrouille, N., Perrett, K., Regnault, N., Rich, J., Taillet, R., Baumont, S., Bronder, J., Ellis, R. S., Filiol, M., Lusset, V., Perlmutter, S., Ripoche, P., & Tao, C. 2006, *ApJ*, 648, 868
- Timmes, F. X., Brown, E. F., & Truran, J. W. 2003, *ApJ*, 590, L83
- Verhulst, P.-F. 1845, *Nouv. mém. de l'Academie Royale des Sci. et Belles-Lettres de Bruxelles*, 18, 1
- Wells, L. A., Phillips, M. M., Suntzeff, B., Heathcote, S. R., Hamuy, M., Navarrete, M., Fernandez, M., Weller, W. G., Schommer, R. A., Kirshner, R. P., Leibundgut, B., Willner, S. P., Pletier, S. P., Schlegel, E. M., Wheeler, J. C., Harkness, R. P., Bell, D. J., Matthews, J. M., Filippenko, A. V., Shields, J. C., Richmond, M. W., Jewitt, D., Luu, J., Tran, H. D., Appleton, P. N., Robson, E. I., Tyson, J. A., Guhathakurta, P., Eder, J. A., Bond, H. E., Potter, M., Veilleux, S., Porter, A. C., Humphreys, R. M., Janes, K. A., Williams, T. B., Costa, E., Ruiz, M. T., Lee, J. T., Lutz, J. H., Rich, R. M., Winkler, P. F., & Tyson, N. D. 1994, *AJ*, 108, 2233

- Wood-Vasey, W. M., Miknaitis, G., Stubbs, C. W., Jha, S., Riess, A. G., Garnavich, P. M., Kirshner, R. P., Aguilera, C., Becker, A. C., Blackman, J. W., Blondin, S., Challis, P., Clocchiatti, A., Conley, A., Covarrubias, R., Davis, T. M., Filippenko, A. V., Foley, R. J., Garg, A., Hicken, M., Krisciunas, K., Leibundgut, B., Li, W., Matheson, T., Miceli, A., Narayan, G., Pignata, G., Prieto, J. L., Rest, A., Salvo, M. E., Schmidt, B. P., Smith, R. C., Sollerman, J., Spyromilio, J., Tonry, J. L., Suntzeff, N. B., & Zenteno, A. 2007, *ApJ*, 666, 694
- Yip, C. W., Connolly, A. J., Szalay, A. S., Budavári, T., SubbaRao, M., Frieman, J. A., Nichol, R. C., Hopkins, A. M., York, D. G., Okamura, S., Brinkmann, J., Csabai, I., Thakar, A. R., Fukugita, M., & Ivezić, Ž. 2004, *AJ*, 128, 585
- Younger, P. F., & van den Bergh, S. 1985, *A&AS*, 61, 365

TABLE 5  
 HIGH- $z$  SN Ia INFORMATION

ESSENCE Name	IAU Name	$z$	Phase <sup>a</sup> (d)	$\Delta^b$	$A_V$ (mag)	Rest Wavelength Range (Å)
b010	2002iy	0.591	-5.0	-0.166	0.104	2517 – 6461
b010	2002iy	0.591	-1.8	-0.166	0.104	2130 – 5832
b010	2002iy	0.591	13.9	-0.166	0.104	3469 – 5933
b010	2002iy	0.591	14.4	-0.166	0.104	2756 – 5605
b013	2002iz	0.426	-1.0	0.034	0.170	2842 – 7190
b013	2002iz	0.426	19.8	0.034	0.170	3085 – 6255
b016	2002ja	0.329	0.1	0.190	0.359	2997 – 7725
b020	2002jr	0.425	-8.4	0.059	0.202	2810 – 7204
b020	2002jr	0.425	12.6	0.059	0.202	3684 – 6610
d033	2003jo	0.531	4.8	-0.322	0.085	2779 – 5833
d058	2003jj	0.583	1.1	-0.470	0.119	2736 – 5641
d083	2003jn	0.333	3.8	-0.273	0.084	3174 – 6699
d084	2003jm	0.519	3.6	-0.197	0.221	2821 – 5879
d085	2003jv	0.401	-0.4	-0.228	0.182	3790 – 6795
d086	2003ju	0.205	-4.8	-0.177	0.628	4929 – 7983
d086	2003ju	0.205	20.9	-0.177	0.628	3070 – 8174
d087	2003jr	0.340	14.7	-0.112	0.126	4044 – 7208
d089	2003jl	0.436	10.2	-0.198	0.134	2973 – 6218
d093	2003js	0.363	-2.8	-0.365	0.077	3117 – 6552
e142	2003js	0.363	15.0	-0.365	0.077	3111 – 6555
d097	2003jt	0.436	4.5	-0.317	0.116	2957 – 6218
d099	2003ji	0.211	18.7	-0.110	0.118	4475 – 7976
d117	2003jw	0.309	-4.7	0.298	0.209	3254 – 6822
d149	2003jy	0.342	-8.1	-0.214	0.170	3182 – 6654
e020	2003kk	0.159	-2.4	-0.034	0.437	3192 – 7592
e029	2003kl	0.332	-1.7	0.219	0.259	2777 – 6606
e121	2003kl	0.332	0.5	0.219	0.259	3021 – 6906
e108	2003km	0.469	-10.8	-0.280	0.071	2518 – 6126
e108	2003km	0.469	-10.1	-0.280	0.071	2566 – 6739
e108	2003km	0.469	-10.1	-0.280	0.071	2952 – 6072
e132	2003kn	0.239	-5.7	-0.128	0.739	3410 – 7211
e136	2003ko	0.352	-1.2	0.332	0.304	3125 – 6609
e138	2003kt	0.612	6.5	-0.284	0.103	2660 – 5543
e140	2003kq	0.631	-1.4	-0.187	0.121	2608 – 5478
e147	2003kp	0.645	1.0	-0.174	0.071	2586 – 5432
e148	2003kr	0.429	-7.1	-0.107	0.102	3010 – 6192
e149	2003ks	0.497	10.7	0.016	0.186	2873 – 5910
f011	2003lh	0.539	7.9	-0.090	0.157	2067 – 6107
f041	2003le	0.561	4.8	-0.301	0.086	2144 – 5952
f076	2003lf	0.410	3.1	0.175	0.227	2601 – 6259
f076	2003lf	0.410	3.1	0.175	0.227	2272 – 6462
f096	2003lm	0.412	3.7	0.171	0.324	2532 – 6575
f216	2003ll	0.599	6.2	-0.104	0.117	2512 – 5809
f231	2003ln	0.619	5.7	-0.247	0.089	2193 – 5752
f235	2003lj	0.422	3.4	0.165	0.133	2365 – 6535
f244	2003li	0.540	5.4	-0.020	0.131	2283 – 6064
f308	...	0.394	0.5	0.031	0.145	2482 – 6271
g005	2004fh	0.218	2.4	-0.253	0.428	2921 – 7602
g050	2003fn	0.633	-1.2	-0.318	0.128	3245 – 5835
g052	2004fm	0.383	-0.5	0.382	0.143	2516 – 6718
g055	2004fk	0.302	5.1	-0.294	1.009	4086 – 7327
g097	...	0.340	10.4	-0.289	0.322	2973 – 6791
g120	2004fo	0.510	-0.9	-0.286	0.186	2203 – 6160
g133	...	0.421	19.5	-0.351	0.452	3743 – 6713
g142	...	0.399	13.8	0.210	0.523	2809 – 6719
g160	2004fs	0.493	9.8	-0.308	0.194	3576 – 6403
g240	...	0.687	9.5	-0.163	0.062	1915 – 5498
h283	2004ha	0.502	1.4	0.090	0.265	2331 – 5872
h300	...	0.687	8.5	-0.279	0.076	1940 – 5503
h311	2004hc	0.750	5.9	-0.491	0.065	2018 – 5300
h319	2004hd	0.495	-5.8	-0.274	0.159	3571 – 6381
h323	2004he	0.603	-0.9	-0.108	0.120	3331 – 5951
h342	2004hf	0.421	11.5	-0.356	0.085	3659 – 7037
h359	2004hi	0.348	11.1	-0.182	0.299	3030 – 5708
h363	2004hh	0.213	3.4	0.065	0.775	4154 – 7666
h364	2004hj	0.344	5.3	-0.006	0.087	2752 – 7293
k396	2004hk	0.271	-5.0	0.843	0.175	3202 – 7633
k425	2004hl	0.274	10.8	-0.021	0.250	2360 – 5767
k429	2004hm	0.181	-1.3	-0.094	0.126	3234 – 8000
k430	2004hn	0.582	0.7	-0.112	0.113	2261 – 5891
k441	2004hq	0.680	2.3	-0.203	0.091	3142 – 5678
k448	2004hr	0.401	0.7	0.003	0.311	2872 – 5888
k485	2004hs	0.416	5.5	-0.230	0.849	2895 – 6207
m026	...	0.653	12.0	-0.201	0.102	3361 – 6215

TABLE 5 — *Continued*

ESSENCE Name	IAU Name	$z$	Phase <sup>a</sup> (d)	$\Delta$ <sup>b</sup>	$A_V$ (mag)	Rest Wavelength Range (Å)
m027	...	0.286	6.6	-0.134	0.362	3383 – 6903
m027	...	0.286	9.1	-0.134	0.362	2690 – 7230
m032	...	0.155	15.4	-0.158	0.092	3688 – 8052
m034	...	0.562	9.2	-0.087	0.130	2786 – 5684
m039	...	0.249	16.9	-0.223	0.507	3482 – 7106
m039	...	0.249	17.1	-0.223	0.507	4191 – 7833
m043	...	0.266	11.4	-0.466	1.033	3436 – 7012
m057	...	0.184	14.1	-0.601	0.218	3673 – 7497
m062	...	0.317	3.7	0.149	0.135	3721 – 7424
m138	...	0.582	-6.7	-0.306	0.073	2750 – 5612
m138	...	0.582	-6.6	-0.306	0.073	3128 – 5877
m138	...	0.582	-5.9	-0.306	0.073	2247 – 5897
m158	...	0.463	10.7	-0.334	0.222	3133 – 4812
m158	...	0.463	11.8	-0.334	0.222	3636 – 6520
m193	...	0.341	6.9	-0.124	0.109	3187 – 5249
m226	...	0.671	13.9	-0.227	0.113	3183 – 5569
n256	...	0.631	6.1	-0.339	0.075	2667 – 5441
n258	...	0.522	6.0	0.032	0.110	2858 – 5831
n263	...	0.368	2.7	0.054	0.075	3181 – 6488
n278	...	0.309	5.6	0.033	0.156	3321 – 6779
n285	...	0.528	13.5	-0.122	0.170	2848 – 5808
n326	...	0.268	-2.7	0.703	0.144	3431 – 6999
n404	...	0.216	-4.3	-0.069	0.694	3575 – 7298
p425	...	0.453	11.3	0.183	0.224	2994 – 6108
p425	...	0.453	12.1	0.183	0.224	3423 – 6399
p454	...	0.695	2.1	-0.276	0.070	2566 – 5236
p455	...	0.284	-10.6	-0.061	0.229	3386 – 6911
p524	...	0.508	9.2	-0.229	0.155	2824 – 4668
p528	...	0.777	4.1	-0.310	0.041	2397 – 3961
p528	...	0.777	5.9	-0.310	0.041	2807 – 5228
p534	...	0.615	-3.4	-0.096	0.107	3094 – 5980
p534	...	0.615	-2.3	-0.096	0.107	3294 – 5736

<sup>a</sup> Rest-frame phase relative to  $B$ -band maximum. <sup>b</sup>  $M_V(t=0) = -19.504 \text{ mag} + 0.736\Delta + 0.182\Delta^2 + 5 \log_{10}(H_0/65)$  (Jha et al. 2007).